CrossMark

Fluid inclusions and He–Ar isotopes in pyrite from the Yinjiagou deposit in the southern margin of the North China Craton: A mantle connection for poly-metallic mineralization

Ming-Tian Zhu [a,*], Lian-Chang Zhang [a], Guang Wu [b], Huai-Yu He [c], Min-Li Cui [a]

[a] Key Laboratory of Mineral Resources, Institute of Geology and Geophysics, Chinese Academy of Sciences, Beijing 100029, China
[b] Institute of Mineral Resources, Chinese Academy of Geological Sciences, Beijing 100037, China
[c] Key Laboratory of the Earth's Deep Interior, Institute of Geology and Geophysics, Chinese Academy of Sciences, Beijing 100029, China

ARTICLE INFO

ABSTRACT

The Yinjiagou poly-metallic deposit is located at the southern margin of the North China Craton (SMNCC). Pyrite, the most economically important mineral, is associated with Cu, Mo, Au, Pb, Zn and Ag mineralization. Two main mineralization stages have been identified and studied: a porphyry stage, including the quartz–molybdenite and quartz–sericite–pyrite (QSP) veins, and a vein stage, including the early and the late (economically most important) pyrite stages.

Three types of fluid inclusions are distinguished in quartz and pyrite, including liquid-rich, vapor-rich biphase (LV) and halite-bearing inclusions. The transmitted and infrared microthermometry produced several results. (1) Each of the three types of fluid inclusions is trapped in the quartz of the porphyry stage, with homogenization temperatures of 335–419 °C and salinities of 4.7–49.6 wt.% NaCl equiv. The coexistence of halite-bearing inclusions and low density, vapor-rich biphase (LV) inclusions indicates that the fluid was boiling. The boiling elevated the Fe and S levels in the hyper-saline fluid, as reflected by the development of pyrite, chalcopyrite and S daughter minerals in the halite-bearing inclusions. (2) The fluid in the early pyrite also displays features characteristic of boiling, with homogenization temperatures of 352–>400 °C and salinities of 3.7–42.4 wt.% NaCl equiv, whereas the late pyrite only contains liquid-rich biphase (LV) inclusions, with homogenization temperatures of 263–354 °C and salinities of 6.0–21.3 wt.% NaCl equiv. The relationship between the decreasing salinity and the corresponding decreasing homogenization temperature clearly indicates extensive mixing and dilution. (3) Finally, the infrared calibration indicates that the impact of infrared light intensity on the microthermometric results for the Yinjiagou pyrite-hosted fluid inclusions is limited. The He–Ar isotopic analysis of the fluid inclusions in the pyrite indicates two different fluid sources that involve abundant mantle input. The ^{3}He/^{4}He ratios in the porphyry stage are relatively uniform, ranging from 1.39 to 1.78 Ra (Ra = 1.39×10^{-6} for air), corresponding to 16–22% mantle ^{4}He contribution. This relatively constant range represents the actual helium isotopic composition of the fluids emanating from the cooling intrusions at depth. The range of ^{3}He/^{4}He ratios in the vein stage is wide, varying from 0.80 to 5.26 Ra, corresponding to 9–65% mantle ^{4}He. The significant variation in the ^{3}He/^{4}He ratios in the vein stage reflects mixing between two fluids.

These data indicate that there are two different fluid sources and separate evolutionary processes for the porphyry and vein stages and support a multi-stage mineralization model. The veinlet molybdenite mineralization was induced by the boiling and associated cooling of a magma-sourced fluid that emanated from intrusions at depth. The QSP veins are likely to be pressure release zones and late fluid flow channels. The early pyrite mineralization may be attributed to the influx of a dominantly mantle-derived fluid with high ^{3}He/^{4}He ratio (5.26 Ra), which is most likely related to a later, more mafic magmatic event. The precipitation of the most economically important pyrite resulted from the mixing and diluting of this mantle-derived fluid with a surface-derived fluid. Additionally, the high ^{3}He/^{4}He ratios indicate a strongly extensional setting, which is most likely related to the Late Jurassic to Early Cretaceous lithospheric modification and thinning of the SMNCC.

* Corresponding author. Tel.: +86 10 82998186.
E-mail address: junrich@mail.iggcas.ac.cn (M.-T. Zhu).

1. Introduction

Much of what we know about the mineralizing fluids of hydrothermal ore deposits is derived from studies of fluid inclusions trapped in gangue minerals, e.g., quartz. The applicability of infrared (IR) fluid inclusion microthermometry to metallic minerals, such as wolframite, sphalerite, domeykite and hematite, reveal discrepancies in the homogenization temperatures and salinities between fluid inclusions in ore minerals and the associated quartz that largely disprove the idea of coprecipitation intergrowth (Campbell and Robinson-Cook, 1987; Richards and Kerrich, 1993b; Hagemann and Lüders, 2003; Kouzmanov et al., 2010). Pyrite, a ubiquitous mineral in most hydrothermal ore deposits, is transparent when imaged by IR light to reveal fluid inclusions and internal features (Campbell et al., 1984; Richards and Kerrich, 1993a; Lüders and Ziemann, 1999; Kouzmanov et al., 2002; Lindaas et al., 2002) and can provide more appropriate information regarding the genesis of mineral deposits.

The significant difference of the helium isotope ratios between the mantle and crustal reservoirs allows them to provide a unique insight into the processes that add mantle volatiles to the continental crust (Andrews, 1985; Burnard et al., 1997; Ballentine et al., 2002). Recently, noble gases from ancient fluids trapped as inclusions in hydrothermal minerals have been extensively employed to trace mantle-sourced fluids, identify fluid origins and constrain their mixing histories during the metallogenesis (Stuart et al., 1995; Burnard et al., 1999; Kendrick et al., 2001; Burnard and Polya, 2004; Zhang L.C. et al., 2008). Pyrite, which displays almost no He loss, is considered to be the perfect host mineral to preserve the primary He–Ar isotope composition of the ore-forming fluids (Stuart et al., 1994; Jean-Baptiste and Fouquet, 1996; Hu et al., 1999). Additionally, both the in $situ$ production and diffusion of ^4He and ^{40}Ar in pyrite and the release of lattice-trapped radiogenic He and Ar during crushing are trivial when compared to the large amounts of He and Ar trapped in fluid inclusions (York et al., 1982; Hu et al., 1998; Kendrick and Burnard, 2013).

The Yinjiagou deposit is tectonically located at the southern margin of the North China Craton (SMNCC) and is part of the East Qinling metallogenic belt, which houses the world's most important Mo ore district and one of the most important gold provinces (Chen et al., 2009; Mao et al., 2011) as well as numerous Pb–Zn–Ag deposits (Fig. 1a). Notably, several important pyrite deposits also occur in this belt, such as the Yinjiagou, Houyaoyu and Luotuoshan deposits. These deposits play an important role in indicating the source of ore materials and investigating the regional tectonic setting. Widely distributed pyrite has a close genetic relationship with porphyry and vein mineralization. In this paper, we report the results of a systematic study of fluid inclusions in quartz and pyrite and of He–Ar isotopic analyses of pyrite from different mineralized veins in Yinjiagou. Our investigation was designed to reveal the characteristics, sources and evolution of ore-forming fluid and to build a possible mineralization model.

2. Geologic background

2.1. District geology

SMNCC is structurally bounded by the Sanmenxia fault with the North China block to the north and by the Tieluzi–Luanchuan fault with the Qinling orogenic belt to the south (Fig. 1a) (Zhang et al., 1996). The Late Archean (ca. 2.6 to 2.9 Ga) Taihua Group (Zhang et al., 2001) forms the crystalline basement, consisting of gneiss, granulite and migmatite, and is disconformably overlain by the Mesoproterozoic (ca. 1.78 Ga) Xiong'er Group, which is arguably part of a large igneous province (Peng et al., 2008; Pirajno et al., 2009) or arc-related volcanic rocks (He et al., 2008). The overlying strata are Mesoproterozoic littoral clastic rocks and carbonate rocks of the Guandaokou Group and Neoproterozoic clastic and carbonate rocks from the shallow marine facies of the Luanchuan Group. Cambrian and Lower Ordovician clastic and carbonate rocks are extensively developed, whereas Upper Ordovician to Lower Carboniferous rocks are absent. Middle–Upper Carboniferous and Permian terrigenous clastic rocks, Triassic clastic rocks from alluvial and fluvial facies, Jurassic continental strata and Cretaceous volcano-sedimentary rocks outcrop sporadically. The Mesozoic is the most significant period for granitoid development in the SMNCC, clustering in the Late Jurassic–Early Cretaceous (148 to 138 Ma) and Early Cretaceous (131 to 112 Ma) (Mao et al., 2008).

Before the Early Triassic, the SMNCC was a relatively stable continental margin on the North China Craton with an Archean crystalline basement and Mesoproterozoic cover structure (Zhu, 1998; Zhang et al., 2001). In the Triassic, the SMNCC was involved in the Qinling orogenic belt forming a series of EW-trending faults (Li et al., 1989; Meng and Zhang, 1999; Ding et al., 2011). Possibly due to the remote westward Pacific subduction (Ren et al., 1992; Zhang et al., 1996; Dong et al., 2011) in the Late Jurassic, the regional tectonic stress of the SMNCC changed to NEE-trending, inducing extensive granitoid emplacement. The Late Jurassic to Early Cretaceous poly-metallic mineralization is attributed to this continental magmatic arc (Ratschbacher et al., 2003; Mao et al., 2011). The intrusions dominate the occurrences of Au deposits and porphyry (skarn) Mo deposits as well as the hydrothermal vein Ag–Pb–Zn deposits (Fig. 1a). Porphyry (skarn) Mo deposits that are spatially associated with Pb–Zn–Ag veins may be part of a larger-scale hydrothermal system, which would provide a useful potential vector for exploration (Mao et al., 2009).

2.2. Ore deposit geology

The Yinjiagou deposit (110°48′40″E, 34°12′21″N) is located at the junction of the NEE-trending Yechangping–Yinjiagou faults and the WE-trending Jizhang–Shipo faults (Fig. 1a). Pyrite, which is the source of sulfur, the main economic product of the mine, is found in close association with Cu, Mo, Au, Pb, Zn and Ag bearing phases. The deposit has a S reserve of 48.8 Mt with an average grade of 20.32%, a Cu metal reserve of 122,000 t with an average grade of 0.46%, and a Mo metal reserve in excess of 6137 t with an average grade of 0.096% (Chen et al., 2007; Zhang X.M. et al., 2008). The outcropping strata in the deposit area are Mesoproterozoic dolomite with interbedded chert. The deposit is hosted by the Yanshanian intrusive complex (Fig. 1b), which has been dated at 148 to 142 Ma (Li et al., 2013). The monzogranite porphyry, the earliest intrusion, is located in the western part of the complex and invaded by the K-feldspar granite porphyry. The rhyolitic tuffs and explosive breccias are locally distributed around the K-feldspar granite porphyry. The quartz diorite porphyry surrounds the northern, eastern and southern margins of the K-feldspar granite porphyry. Zhang X.M. et al. (2008) considered the quartz diorite porphyry as the marginal face of the K-feldspar granite porphyry, without any obvious boundary line. The latest biotite ivernite cuts through all of these intrusions. Both the K-feldspar granite and quartz diorite porphyries are closely related to the Mo, Cu, Au and pyrite mineralization (Fig. 1c and d). Potassic and pyrite-phyllic alterations and pyritization (Fig. 1c and d) occur pervasively and are overprinted by advanced argillic alteration. Skarnization occurs in some of the contact zones with dolomite.

Multiple mineralization stages developed and formed various mineralized veins. Generally, three stages have been identified and are described in chronological and spatial order. (1) The porphyry stage contains molybdenite veinlets and quartz–sericite–pyrite (QSP) ± chalcopyrite ± chalcocite veins. The molybdenite veinlets occur in the K-feldspar granite porphyry (Fig. 1b and d). Disseminated molybdenite in quartz–molybdenite (Q–Mo) ± pyrite veins commonly occurs in multiple bands, often with parallel quartz, displaying a co-depositional character (Fig. 2a). Hence, the fluid inclusions in quartz should represent the fluid responsible for the molybdenum mineralization. Pyrite, where present, is commonly located along the edges of the veins. QSP veins with thicknesses of several centimeters to several
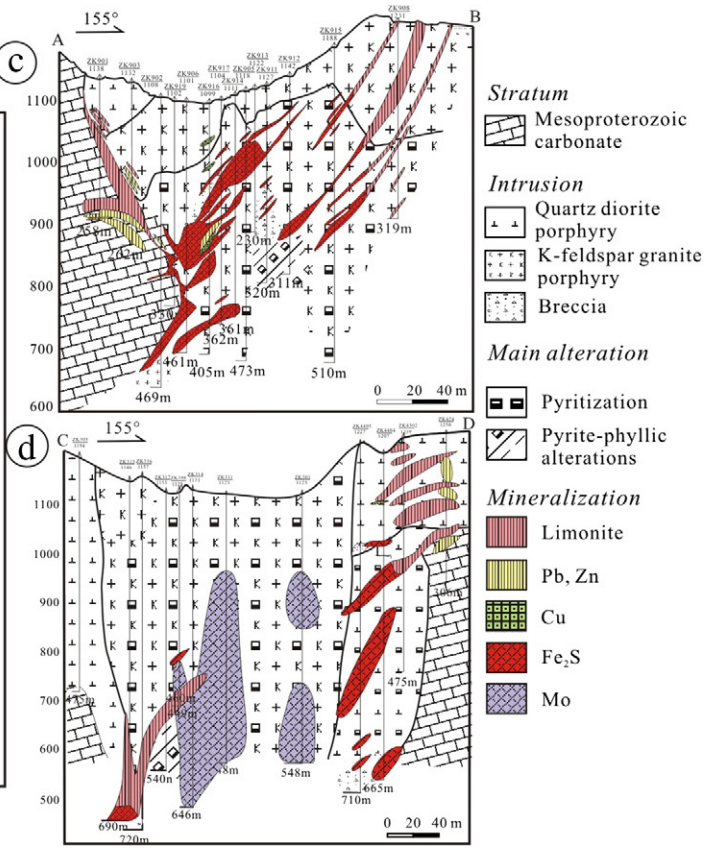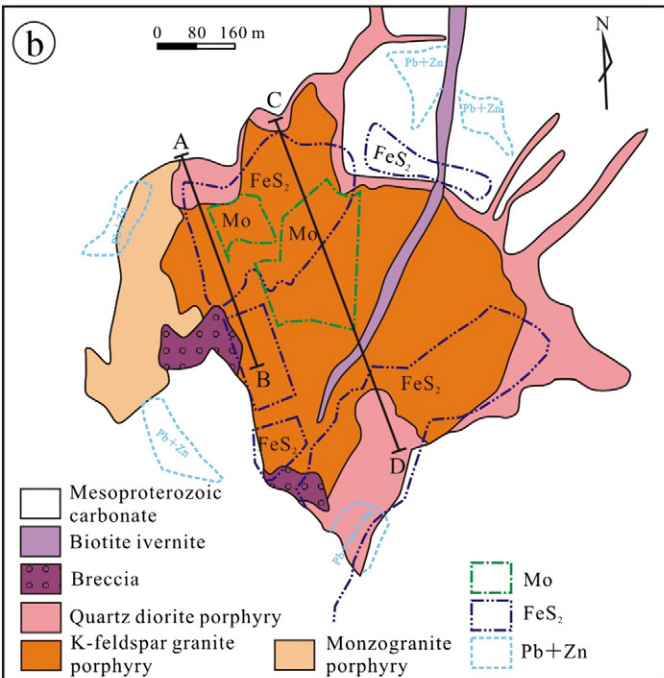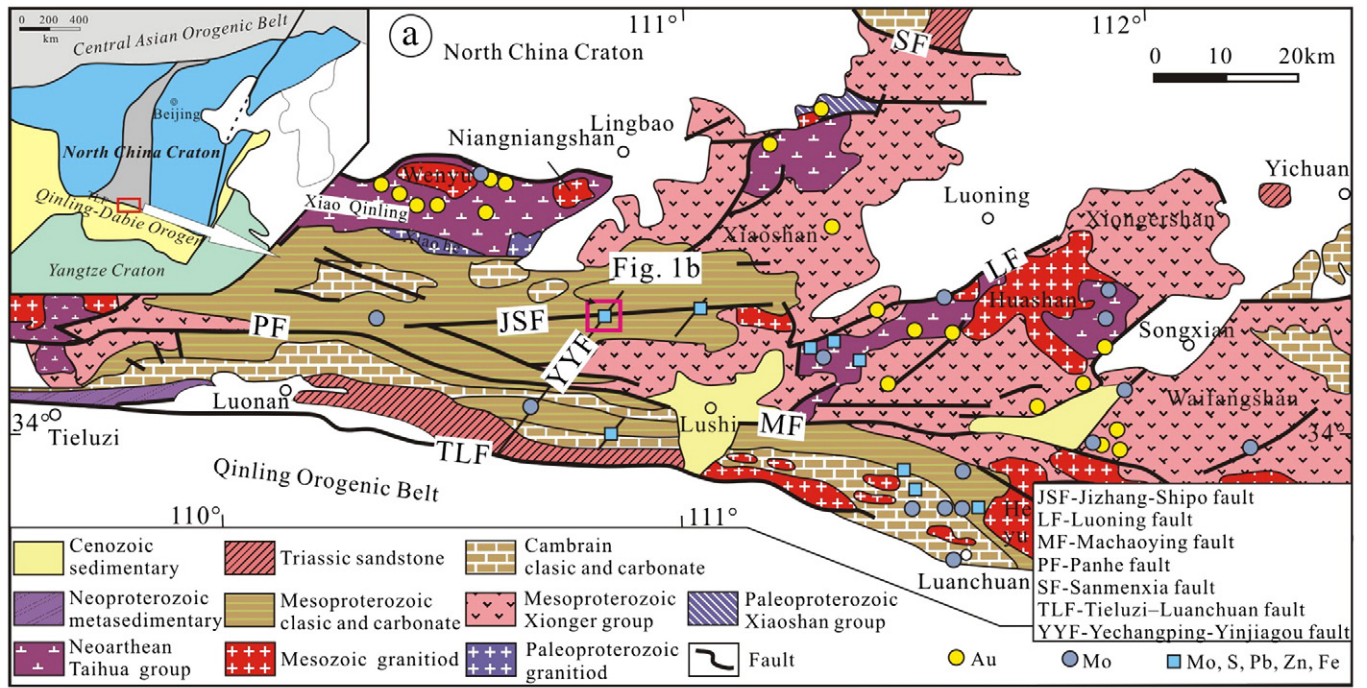
Fig. 1. Regional geological map of the northern margin of the North China Craton (a) (after Luo et al., 1991; Li et al., 2007), local geological (b) and section maps (c and d) of the Yinjiagou deposits.

meters contain less than 20 vol.% sulfide (Fig. 2b), corresponding to the pyrite-phyllic alteration (Fig. 1c and d). These veins, which occur intensively at the roof and floor of the molybdenite and pyrite ore bodies, represent the fracture zones within the granitoids from multi-fracturing events. Quartz occurs as isolated grains and is commonly intergrown with pyrite (Fig. 2b), most likely representing a paragenetic relationship.

(2) The veined pyrite ± quartz ± calcite ± chalcopyrite ± chalcocite stage, with thicknesses of several meters to tens of meters, is located in the K-feldspar granite and quartz diorite porphyries, and is locally in the contact zones with dolomite. Pyrite commonly oxidizes to iron hydroxide in the shallow and fault zones (Fig. 1b–d). At least two generations of pyrite were identified based on the mineral assemblages and fluid
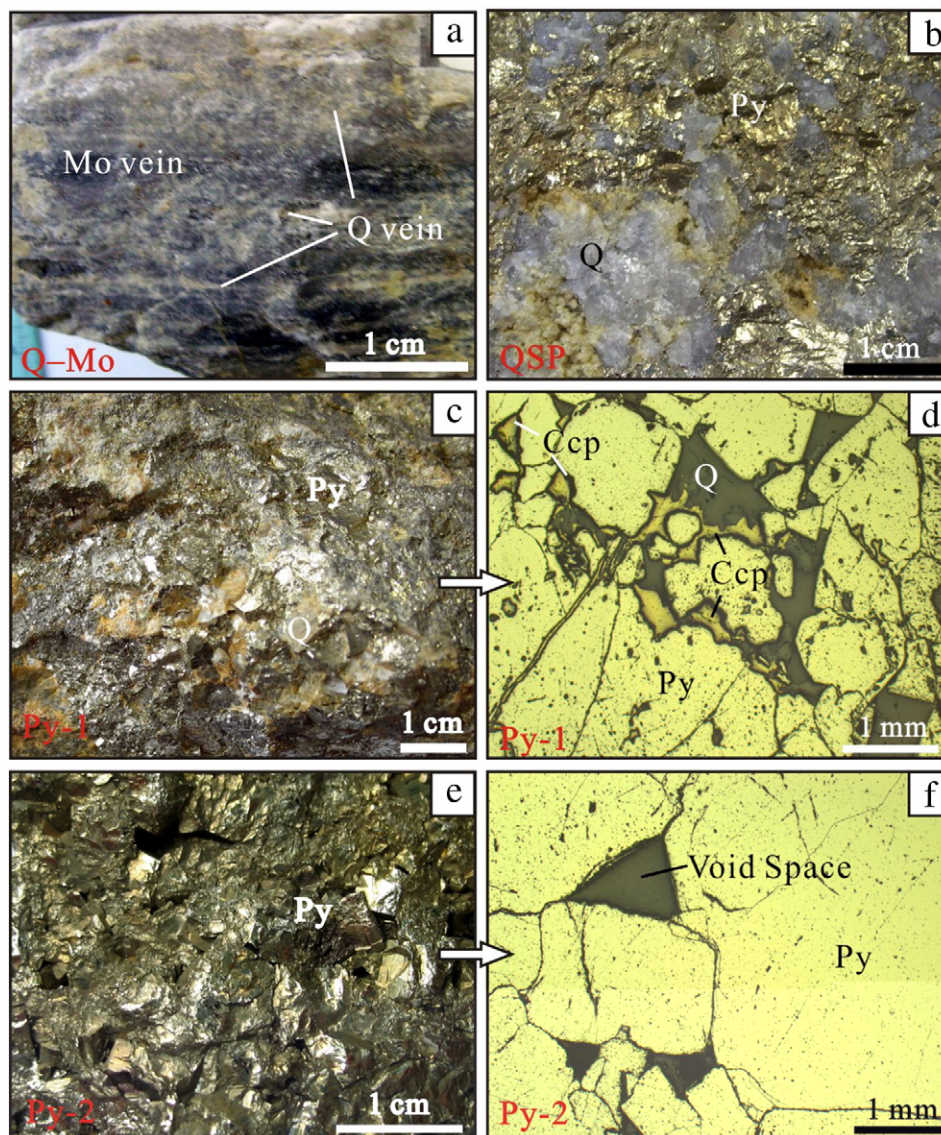
Fig. 2. Typical Photographs of the main mineralized veins from the Yinjiagou deposit. Quartz–molybdenite (Q–Mo) vein shows interbedded co-depositional character (a). Quartz is intergrown with pyrite (Py) in the quartz–sericite–pyrite (QSP) vein (b). Quartz in an early pyrite (Py-1) vein occurs as isolated grains (c). Pyrite surrounds chalcopyrite (Ccp) in Py-1 under reflected light (d). Late pyrite (Py-2) occurs as euhedral crystals (e). Void space within Py-2 grains suggests enough growing space (f).

inclusion characteristics. The early pyrite (Py-1) is found in pyrite–quartz–chalcopyrite ± chalcocite assemblages. Quartz occurs as isolated grains wrapped by pyrite (Fig. 2c). Chalcopyrite is distributed along micro-fractures within pyrite (Fig. 2d) or occurs in the pyrite grains. The late pyrite (Py-2) is found in pyrite ± quartz ± chalcopyrite ± calcite assemblages, representing the most economically important ore bodies. Py-1, usually with a fragmented texture, is contained within Py-2 in some cases. The abundant void space between pyrite grains (Fig. 2e and f) indicates that pyrite had sufficient growing space. (3) Distal quartz–Pb and Zn veins are predominantly distributed within the faults and interstratified cracks of dolomite, especially at the junctions of two fractures, and can extend to several kilometers around the intrusions (Fig. 1b). This study generally focuses on the first two stages.

3. Sample preparation and methods

3.1. Sample preparation

The samples that were examined for the fluid inclusion study were representative of the veins described above, including the Q–Mo, QSP, Py-1 and Py-2 veins that were collected from the mine trenches 100 to 250 m below the present surface. Thirty inclusion sections of pyrite, including cubic, octahedral, granular, fragmented and massive crystals, were prepared, and their thicknesses ranged between 100 and 200 μm, which was thinner than the five quartz sections of approximately 300 μm. Only eight pyrite sections of Py-1 and Py-2 had adequate transparency and were, thus, chosen for further IR microthermometry. A good polish on both surfaces of the samples is required to optimize the transparency due to the high refractive index contrast between pyrite and air. Note that in the following text, tables and figures, we use the labels Q–Mo (Q) and QSP (Q) for the quartz in the Q–Mo and QSP veins, respectively, and Q–Mo (Py) and QSP (Py) for the pyrite in the Q–Mo and QSP veins, respectively.

Pyrite grains for the He–Ar isotopic analyses were selected from the Q–Mo, QSP, Py-1 and Py-2 veins. Coarsely crushed chips were washed ultrasonically in methanol, sieved and handpicked under a binocular microscope. Fresh crystals of 20–40 (450–850 μm) mesh fractions were selected by hand. The grains were then rinsed with distilled water and dried. Approximately 1 g of sample was load into an in vacuo one-step crusher.

3.2. Equipment of microthermometry

Optical observations and microthermometry of fluid inclusions in quartz were conducted using a Linkam THMSG 600 heating and freezing stage at the Key Laboratory of Mineral Resources, Institute of Geology and Geophysics, Chinese Academy of Sciences (IGGCAS). Apparent salinities of the natural fluid inclusions are reported in wt.% NaCl equiv, based on the halite dissolution temperatures for halite-bearing inclusions (Hall et al., 1988) and the final ice melting temperatures for biphase (LV) inclusions (Bodnar, 1993).

Optical observations and microthermometry of fluid inclusions in pyrite were conducted using an Olympus BX51 microscope equipped for IR-microscopy at the State Key Laboratory of Geological Processes and Mineral Resources, China University of Geosciences (Wuhan). A long-working-distance IR objective (Olympus MIRPlan 50×) is used. An IR-sensitive Hamamatsu C274–03/ER camera, with a quoted spectral response of 0.4–2.2 μm, is mounted on a trinocular head assembly, which allows the observation of phase changes on a TV monitor. Microthermometric measurements of pyrite-hosted fluid inclusions were conducted using a Linkam MDS 600 heating and freezing stage. Due to the strong IR absorption above 350 to 400 °C, the cycling heating method, similar to the cyclic method described by Goldstein and Reynolds (1994), was performed in order to obtain the homogenization temperatures and salinities of fluid inclusions in pyrite.

3.3. Methods of He–Ar isotopic analysis

He–Ar isotopic analysis was conducted with the one-step crushing technique at the Key Laboratory of the Earth's Deep Interior, IGGCAS. Crusher was constructed from 316 L stainless steel and the noble gas isotope analyses were performed on a Noblesse mass spectrometer in static mode. The detailed crushing and analytical procedures have been described by He et al. (2011). Helium blanks were negligible (^{3}He blank $< 3 \times 10^{-17}$ cm^3 STP); and Ar blanks were small, about 0.1% relative to the signals. The air standard, whose ^{3}He/^{4}He ratio is 1.39×10^{-6} (Ra) and ^{40}Ar/^{36}Ar ratio is 298.5, was measured every two weeks. The uncertainty of the average ^{3}He/^{4}He ratio of calibration measurements is better than 5%, thus 5% error was assigned to the calculated ^{3}He/^{4}He ratio and this error was included in the unknown sample correction. The sample results were normalized to the value of the air standard and corrected for system blanks.

4. Results

4.1. Fluid inclusion petrography

4.1.1. Types of fluid inclusions

In general, three types of fluid inclusions are distinguished (Fig. 3). The classification of fluid inclusion types observed in this study is primarily based on the phase proportions at room temperature. Where groups or clusters of inclusions exhibit similar heating and freezing behaviors, we infer that they were trapped in a homogeneous fluid and that the inclusions have not experienced significant post-trapping modification (Goldstein and Reynolds, 1994). Some fluid inclusions in the pyrite are isolated, representing primary inclusions, and some are distributed along the growth banding, suggesting a pseudosecondary origin.

Liquid-rich (L type) biphase (LV) inclusions occur as negative, irregularly-shaped to rounded inclusions and usually range from 5 to 80 μm. No liquid CO$_2$ was observed. Vapor bubbles occupy approximately 5 to 40% of the inclusion volume and homogenize to liquid. L type inclusions are common in every mineralized vein, especially in Py-2, where only L type inclusions were observed (Fig. 3g–i).

Vapor-rich (V type) biphase (LV) inclusions have negative crystalline or round shapes and range from 7 to 50 μm in size. Vapor bubbles occupy more than 50% of the inclusion volume and homogenize to vapor on heating. No daughter crystals or liquid CO$_2$ were observed.

Halite-bearing (H type) inclusions generally have round, isometric or negative crystalline shapes and are typically between 6 and 40 μm in size. H type inclusions contain well-formed cubic halite and generally several other daughter minerals, such as round sylvite, high relief calcite and plated anhydrite (Fig. 3a–f). Opaque daughter minerals commonly occur as round shapes, and are identified as pyrite, chalcopyrite using Raman spectrometry on quartz (Fig. 4) and sulfur by Scanning Electron Microscopy on the cavity of the fluid inclusions in the pyrite (not shown). The vapor bubbles occupy approximately 5 to 30% of the inclusion volume. Anhydrite, calcite and opaque daughter minerals did not dissolve when heated to temperatures in excess of 550 °C. Sylvite usually dissolved earlier than halite, and, thus, the salinities are calculated from the halite dissolution temperatures.

Fig. 4 shows the results of the laser Raman spectrum of daughter minerals in Q–Mo (Q) and QSP (Q). We first determined the peak values of pyrite grains (crystals) (Fig. 4a) and then compared these with the values we obtained from the opaque daughter minerals in H type inclusions. The results show that some opaque daughter minerals are pyrite and chalcopyrite (Fig. 4b and c), and some transparent minerals are calcite (Fig. 4c). According to the laser Raman analysis, CO$_2$ is present in the vapor of some L and V type inclusions in the quartz (not shown), but the content is usually insufficient (less than 0.8 mol% CO$_2$ calculated from the laser Raman data) to form discrete liquid CO$_2$ at room temperature (Hedenquist and Henley, 1985). The presence of CO$_2$ is also demonstrated by the melting of clathrate between 8.1 and 9.0 °C in some L type inclusions in Py-2. The salinities derived from the ice melting temperatures are much higher than those derived from the clathrate melting temperatures.

4.1.2. Transparency of pyrite

Pyrite was commonly transparent or displayed patched or zoned transparency under the IR light source (Richards and Kerrich, 1993a); this result is attributed to the crystalline shape and growth environment of pyrite. The transparency of euhedral pyrites is much better than that of the anhedral and fine grained pyrites because fine-grained aggregates contain numerous planes oblique to the section, and these planes considerably decrease the IR transparency. Different parts of the same pyrite section also have different IR transmittance properties, which may be caused either by the nonuniform distribution of some of the most common elements that can be incorporated into the pyrite lattice to form extensive solid solutions (Richards and Kerrich, 1993a; Kouzmanov et al., 2002) or other mineral inclusions trapped within the pyrite. Additionally, late deformation can fragment the pyrite and lead to brittle or plastic slide along the crystal plane (Boyle et al., 1998), inducing the IR opacity of pyrite in some cases. During heating, the transmittance of the pyrite gradually decreased, caused by a gradual shift of the main absorption edge of pyrite towards longer wavelengths (Lindaas et al., 2002). Freezing has practically no influence on the IR transparency.

4.1.3. Fluid inclusions in pyrite

The fluid inclusion size in the pyrite is usually large and can reach 200 μm. Most fluid inclusions occur in clusters and have elongated shapes (Fig. 3d–h) and some are distributed along the growth banding of pyrite (Fig. 3h), most likely suggesting primary or pseudosecondary origins. Pyrite has more opaque inclusions than transparent inclusions. The opacity is attributed to a high refractive index contrast between pyrite and the trapped aqueous fluid (Richards and Kerrich, 1993a), resulting in the intense refraction of light. Lüders and Ziemann (1999) suggested that the post-entrapment reactions of the fluid with the host-mineral induced the precipitation of a solid phase on the inclusion walls, and this rim absorbs near-IR light and causes the inclusions to be opaque. However, this idea was rejected by Philippot et al. (2000), who noted that the relatively homogeneous distribution of most elements
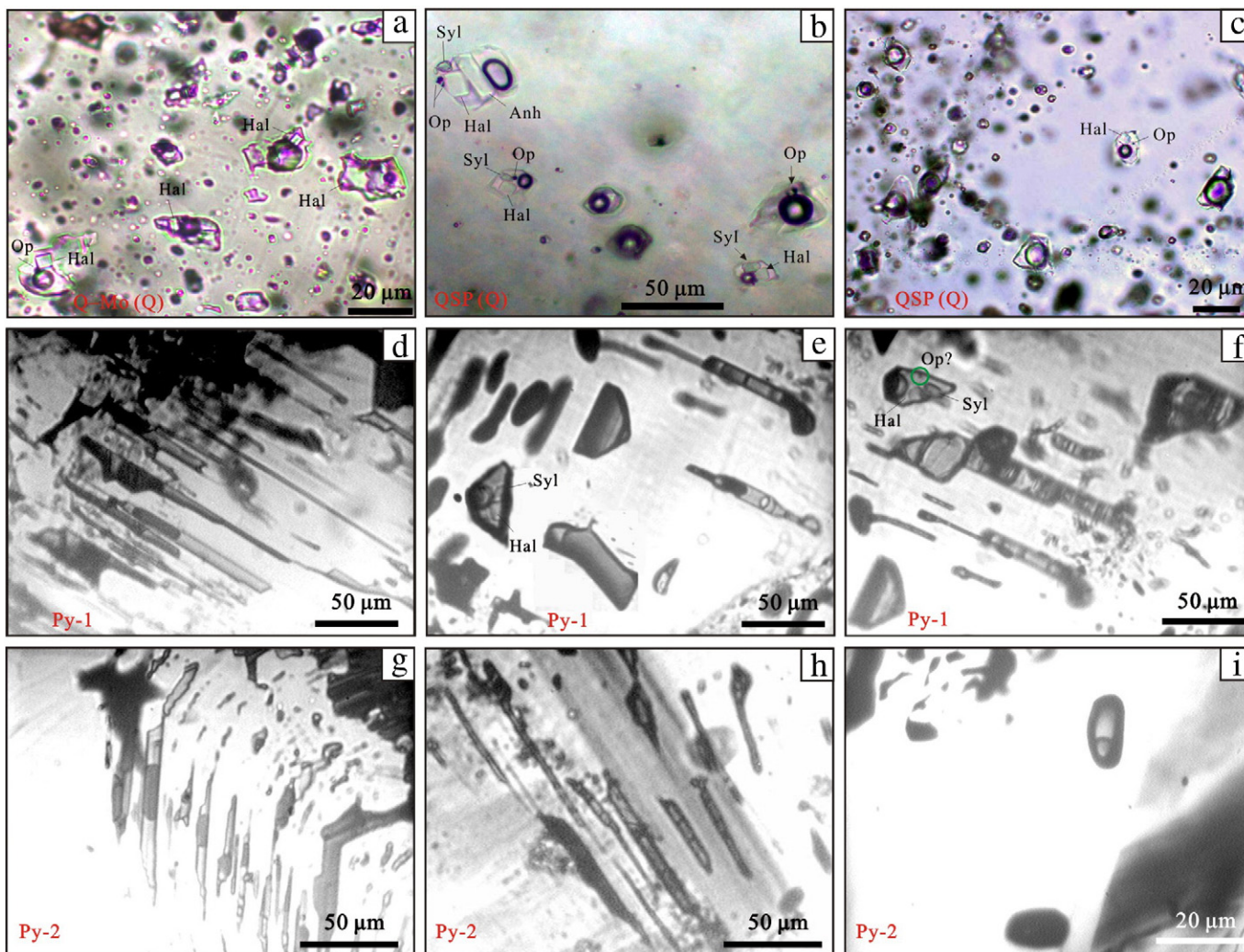
Fig. 3. Transmitted (a–c) and infrared light (d–i) photomicrographs of fluid inclusions from the Yinjiagou deposit. Coexistence of vapor-rich biphase (LV) and halite-bearing inclusions hosted in the Q–Mo (Q) suggests boiling (a). Daughter mineral is usually cubic halite (Hal) and opaque (Op) daughter mineral is pyrite. Fluid inclusions hosted in the QSP (Q) also suggest boiling; Halite-bearing inclusions contain daughter minerals of cubic halite, rounded sylvite (Syl) and plated anhydrite (Anh) as well as opaque pyrite and chalcopyrite (b and c). Liquid-rich biphase (LV) inclusions in early pyrite (Py-1) show unobvious phase change during cooling and heating (d). Coexistence of vapor-rich biphase (LV) and halite-bearing inclusions in Py-1, with perfect infrared light transparence, suggest boiling (e and f). Liquid-rich biphase (LV) inclusions in Py-2 show typical stretching texture (g) and occur along growth banding (h) or in isolation (i).

throughout the inclusion argues against the presence of minute, optically invisible compounds that are precipitated inside the inclusion. The nonopaque and opaque fluid inclusions can coexist even within the same view of the pyrite (Fig. 3e and f), indicating that some opaque inclusions may simply be vapor-rich, vapor or halite-bearing inclusions that share similar fluid characteristics. The complex morphology is an important cause of the total internal light reflections, thus resulting in the partial or complete opacity of the fluid inclusion (Fig. 3d–f) as described by Kouzmanov et al. (2002). Considering the widths of 100 to 200 μm for the doubly polished sections and the sizes of approximately 200 μm for some fluid inclusions, some opaque fluid inclusions may simply be the empty cavities with their roofs removed. Where cavities intersect the surface of the section, the daughter minerals were determined to be NaCl, KCl and sulfur by Scanning Electron Microscopy.

4.2. Results of microthermometry and calibration for pyrite

4.2.1. Microthermometry

The microthermometric results of different types of fluid inclusions in different types of veins are presented in Table 1 and Figs. 5 and 6. Note that the salinities and homogenization temperatures of the V type inclusions are difficult to determine and the presented values are approximate.

4.2.1.1. Transmitted microthermometry of quartz-hosted fluid inclusions. Q–Mo (Q) has L, V and H type inclusions (Fig. 3a). The salinities of the L type inclusions vary from 14.1 to 19.2 wt.% NaCl equiv, with homogenization temperatures ranging from 378 to 416 °C. The V type inclusions homogenize between 395 and 402 °C and no ice melting temperatures are determined. The H type inclusions completely homogenize by vapor bubble disappearance from 389 to 402 °C and have salinities ranging from 39.1 to 40.8 wt.% NaCl equiv (Fig. 5a).

QSP (Q) hosts L, V and H type inclusions (Fig. 3b–c). L type inclusions have salinities ranging from 14.5 to 15.5 wt.% NaCl equiv and homogenize between 335 and 377 °C. The salinities of the V type inclusions range from 4.7 to 7.3 wt.% NaCl equiv and homogenization temperatures vary from 359 to 419 °C. Some of the H type inclusions completely homogenize when vapor dissolves into the liquid phase from 340 to 379 °C, with salinities ranging from 33.7 to 35.7 wt.% NaCl equiv. Others homogenize when halite dissolves into the liquid phase between 397 and 419 °C, with salinities ranging from 47.2 to 49.6 wt.% NaCl equiv (Fig. 5b).
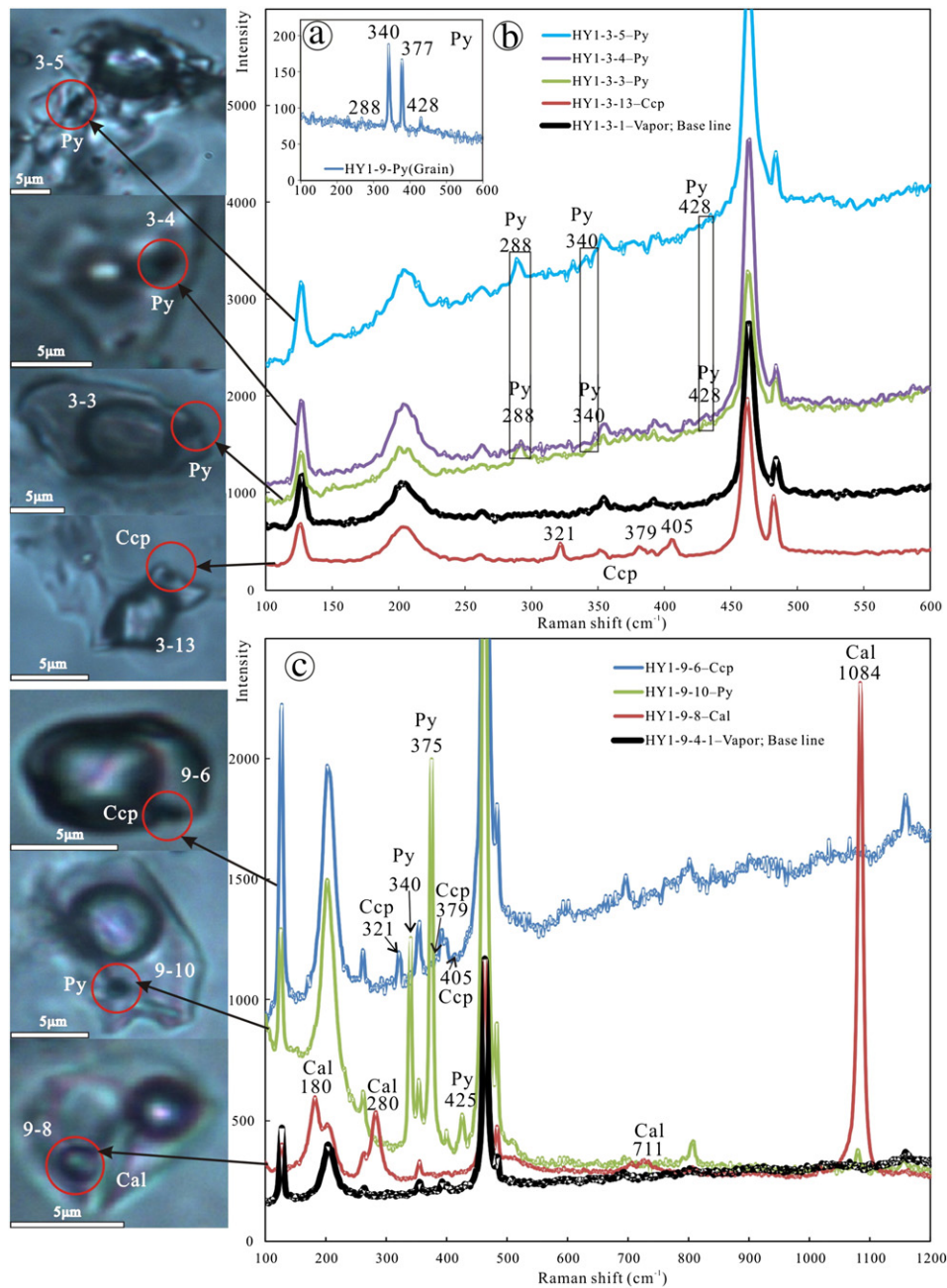
Fig. 4. Laser Raman analyses of pyrite grain (a) and halite-bearing inclusions in Q– Mo (Q) (b) and QSP (Q) (c). Pyrite grain shows typical Raman spectrum of pyrite (a). Daughter minerals are distinguished as opaque pyrite (Py), chalcopyrite (Ccp) (b and c) and transparent calcite (Cal) (c).

4.2.1.2. Infrared microthermometry of pyrite-hosted fluid inclusions. Py-1 contains L, V and H type inclusions (Fig. 3d–f). Despite the fact that cooling had almost no impact on the transmittance of fluid inclusions, the phase change for some L type inclusions was not obvious (Fig. 3d). The apparent salinities of several L type inclusions vary from 4.2 to 6.4 wt.% NaCl equiv. During heating to greater than 350 °C, most of the L type inclusions could not homogenize and were opaque, whereas some homogenize between 361 and 367 °C. The V type inclusions have salinities ranging from 3.7 to 7.3 wt.% NaCl equiv and homogenize between 352 and >370 °C. The H type inclusions have salinities ranging from 36.8 to 42.4 wt.% NaCl equiv. Complete homogenization temperatures range from 372 to >400 °C as vapor dissolves into the liquid phase (Fig. 5c).

Py-2 hosts only L type inclusions. However, the possibility of the presence of V type inclusions cannot be entirely excluded from some dark inclusions. L type inclusions have large ranges of salinities from

6.0 to 21.3 wt.% NaCl equiv, with homogenization temperatures ranging from 263 to 354 °C (Fig. 5d).

To summarize, the microthermometric results (Figs. 5 and 6) indicate that quartz of the porphyry stage contains various types of fluid inclusions and has relatively high and much larger ranges of homogenization temperatures and salinities. The Py-1 fluid characteristics are similar to those of quartz inclusions of the porphyry stage, but quite different from those of Py-2 pyrites, which only contains L type inclusions with variable salinities and homogenization temperatures.

4.2.2. Temperature calibration for pyrite
Campbell and Robinson-Cook (1987) reported that no difference in microthermometric results was found between the visible light and IR light sources during the heating and freezing runs for wolframite, whereas Moritz (2006) suggested that the IR light source intensity affects the microthermometry results for some opaque

Table 1
Microthermometric results from the Yinjiagou deposit.

	FI type	Size (µm)	$T_{m, Hal}$ (°C) (N)	Salinity (Wt.% NaCl equiv) (N)	T_{total} (°C) (N)
Q–Mo (Q)					
HY1-7	L			14.1–19.2 (14)	378–416 (19)
	V			n. m.	395–402 (5)[a]
	H		312–333 (2)	39.1–40.8 (2)	389–402 (2)
QSP (Q)					
HY1-9	L	5–13		14.5–15.5 (5)	335–377 (14)
	V	7–12		4.7–7.3 (8)[a]	359–419 (8)[a]
	H	6–10	235–419 (13)	33.7–49.6 (13)	340–417 (12)
Py-1					
HY3-7	L	20–70		4.2–6.4 (4)	361–>420 (13)[b]
	V	40–50		3.7–7.2 (3)[a]	352–>370 (3)[b]
	H	35–40	281–350 (3)	36.8–42.4 (3)	372–>400 (3)[b]
Py-2					
HY3-4	L	40–50		19.4–20.0 (2)	282–295 (2)
HY3-5	L	10–50		15.6–21.3 (5)	305–354 (7)
HY3-10	L	10–80		15.5–16.0 (2)	290–352 (4)
HY3-14	L	30–40		6.0–16.6 (15)	263–336 (20)
HY21-1	L	20–40		14.5–19.8 (5)	278–341 (5)
HY21-2	L	15–50		13.9–20.6 (5)	307–324 (5)
HY23-7	L	10–30		15.2–18.8 (4)	303–334 (5)

L, V and H FI are types of liquid-rich, vapor-rich biphase (LV) and halite-bearing fluid inclusions, respectively. $T_{m, Hal}$ and T_{total} represent the halite dissolution temperature and the complete homogenization temperature, respectively. n.m.: salinity is not determined due to unobvious phase change when cooling.

[a] Homogenization temperatures and salinities are approximate values owing to difficulties in observing phase boundaries on vapor-rich inclusions.

[b] Uncertainty of homogenization temperatures of fluid inclusions in Py-1 is greatest owing to the infrared opacity under high temperatures.

minerals, e.g., enargite, leading to an overestimate of fluid salinities and an underestimate of homogenization temperatures. A similar conclusion has been reported by Ge et al. (2011). There have been no available data reported to determine the impact of the IR light intensity for pyrite to date.

We chose several L type inclusions, between 40 and 80 µm in size, to verify this potential problem in pyrite. The analytical results are listed in Table 2. The relative IR light intensities (2, 4, 6, 8, 10 and 12) are controlled by the adjusting knob and approximately equal to the voltage values displayed by the LED indicator, and each of the IR light intensities corresponds to a salinity and/or homogenization temperature. The results indicate that the variation in ice melting temperatures is less than −0.3 °C (Fig. 7a) and that in homogenization temperatures ranges from 0.3 °C to 1.3 °C (Fig. 7b). Given the instrumental, analytical and associated errors, we consider the influence of IR light intensity on the microthermometry of fluid inclusions in pyrite to be negligible.

4.3. Results of He–Ar isotopic analyses

The He–Ar analytical results (Table 3) indicate that the $^4He/^4He$ ratios of fluid inclusions in pyrite range from 0.80 to 5.26 Ra; in contrast, there is a considerable range in $^{40}Ar/^{36}Ar$, from 421 to 1095. ^4He concentrations in the pyrites are $5.33–83.78 \times 10^{-9}$ cm³ STP g^{-1}, whereas Ar concentrations are in the range of $2.26–25.28 \times 10^{-9}$ cm³ STP ^{40}Ar g^{-1}.

The variation in the amounts of helium and argon released by duplicate extractions of the same sample (Table 3) may have resulted from heterogeneous distribution of fluid inclusions in pyrite rather than from crushing processes, which is consistent with the petrographic observation that the distribution of fluid inclusions is nonuniform for each section, even for different parts of the same section (Fig. 3d–i). The $^3He/^4He$ ratios of the different crushes remained essentially constant (within 0.1 Ra), regardless of the amount of ^4He released (Fig. 8a), demonstrating that the He isotopic composition of the fluid trapped in the inclusions was homogeneous and that diffusion and in situ ^4He production were not important. The atmospheric He contribution can be determined from the F^4He values (Kendrick et al., 2001),
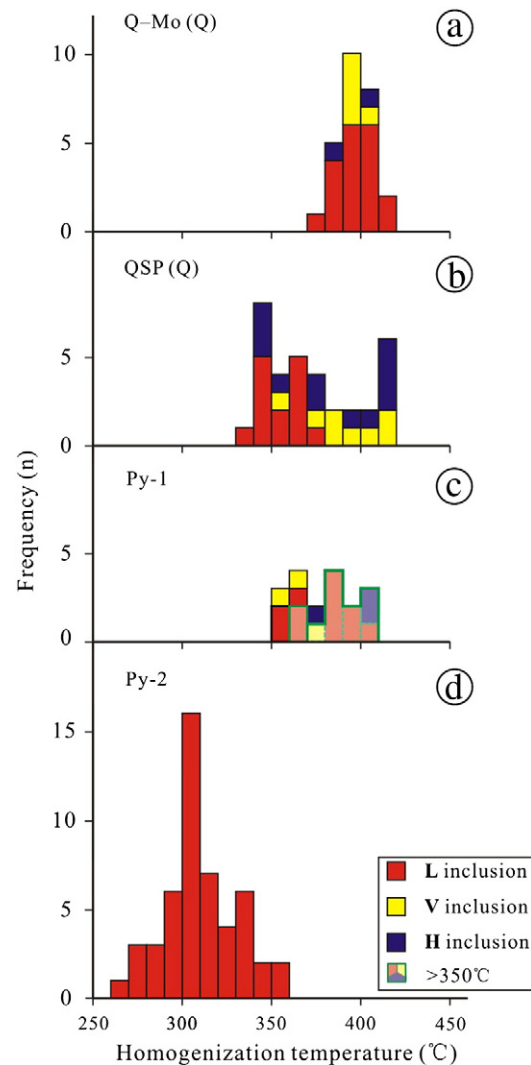

Fig. 5. Histograms of fluid inclusion homogenization temperatures hosted in the Q–Mo (Q) (a), QSP (Q) (b), Py-1 (c) and Py-2 (d) from the Yinjiagou deposit. The uncertainty of temperatures from Py-1 is greatest owing to the infrared opacity under high temperatures.

defined as the $^4He/^{36}Ar$ of a sample relative to the atmospheric $^4He/^{36}Ar$ value of 0.1727 (Sano et al., 2013). The high F^4He values of 1861–20,892 for the pyrite are evidence that the fluids contain negligible contributions of atmospheric He. $^{40}Ar/^{36}Ar$ ratios of 421–1095 are significantly higher than that of air (298.5), consistent with the very limited amount of atmospheric contamination inferred from the F^4He values.

5. Discussion and interpretation

5.1. Fluid characteristics of various veins

Boiling and mixing are the two principal physical processes affecting mineral deposition in geothermal systems (Giggenbach and Stewart, 1982). The unmixing of supercritical $H_2O–NaCl$ fluids into a high density brine and a low salinity, low-density vapor has been recognized in many magmatic–hydrothermal mineralized systems (Audétat and Pettke, 2003; Redmond et al., 2004; Chen and Wang, 2010). In the Yinjiagou deposit, the quartz of the porphyry stage and the Py-1 of the vein stage have identical fluid inclusion assemblages and similar fluid characteristics (Fig. 6). The intermediate density and salinity fluid reflected by the L type inclusions of the porphyry stage might represent the initial fluid compositions. The coexistence of halite-saturated
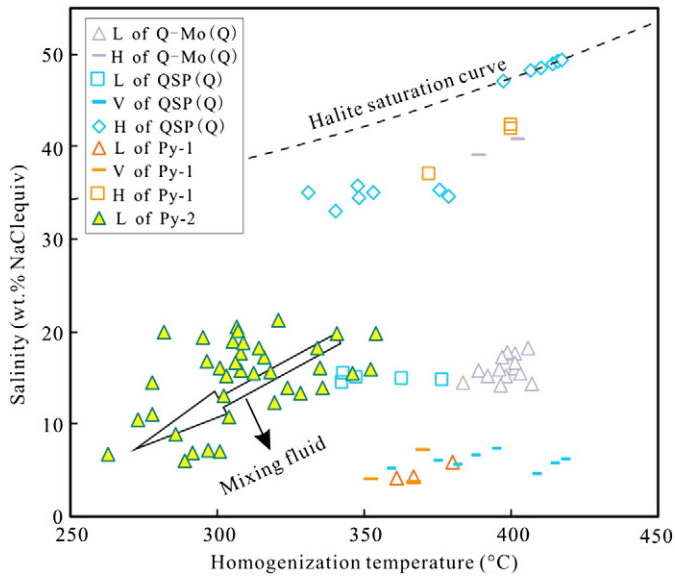
Fig. 6. Homogenization temperature vs. salinity of fluid inclusions from the Yinjiagou deposit. Halite saturation curve based on Driesner and Heinrich (2007). L, V and H are liquid-rich, vapor-rich biphase (LV) and halite-bearing fluid inclusions. The uncertainty of temperatures from Py-1 is greatest owing to the infrared opacity under high temperatures. Coupled decrease in salinity and homogenization temperature shown by the large arrow clearly indicates a mixing fluid of Py-2, evidence that a hot, saline fluid mixed with a cooler, more dilute fluid at temperatures up to 350 °C.

liquid inclusions (H type) and V type inclusions, even in the same grain (Fig. 3a–f), indicates that the fluids were boiling (Bodnar, 1985) throughout the period from quartz–molybdenite vein formation through to early pyrite deposition. The presence of explosive breccia in the K-feldspar granite porphyry with molybdenite mineralization is evidence of sharp pressure drops. These may have led to the boiling. The H type inclusions are considered to have trapped saturated immiscible fluid during the boiling (Shepherd et al., 1985).

With regard to the fluid of Py-2, the relationship between the decrease in salinity from 21 to 6 wt.% NaCl equiv and the corresponding decrease in homogenization temperature from 354 to 263 °C (Fig. 6) clearly indicates a trend of strong dilution, evidence that a hot, saline fluid mixed with a cooler, more dilute fluid. Considering the paragenetic sequence of mineralization and the fluid features of various veins, the hot, saline fluid is likely to be the residue of the early boiling fluid, mixing with groundwater at temperatures up to 350 °C.

Recent experiments and microanalysis for single fluid inclusions demonstrate that phase separation between coexisting vapor and hyper-saline liquid phases can be an important step in the segregation of elements, with the tendency of some elements, including Fe, Zn, Pb and Mn to partition into the brine, while other elements, such as Cu, Au and As in HS complexes, partitioning into the vapor phase (Heinrich et al., 1999; Simon et al., 2004; Pokrovski et al., 2005; Simon et al., 2005; Williams-Jones and Heinrich, 2005; Seo et al., 2009). In the Yinjiagou deposit, H type inclusions containing plenty of opaque pyrite and sulfur are widely distributed in both the porphyry
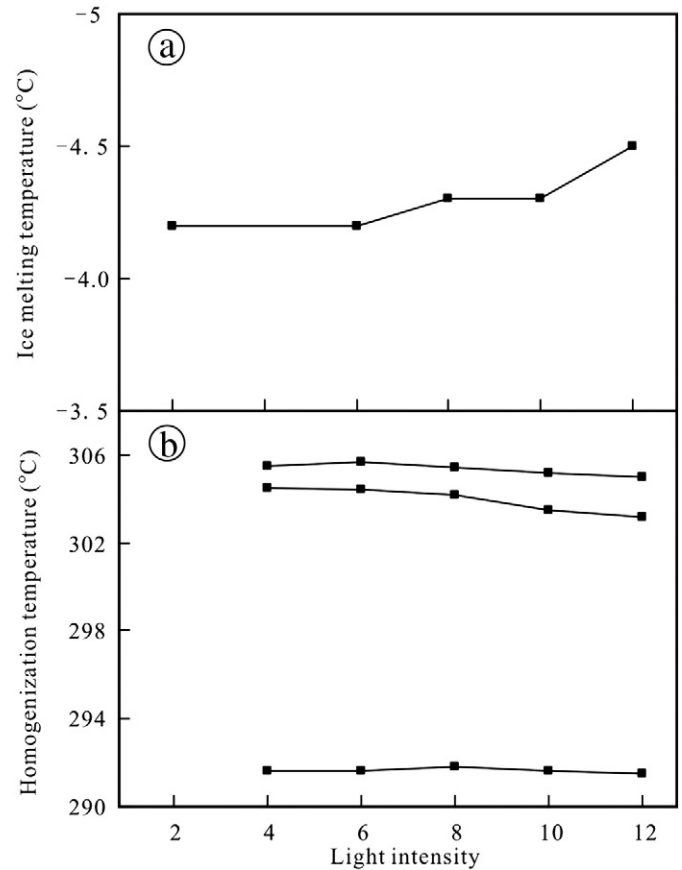

Fig. 7. Effects of infrared light intensity on ice melting temperatures (a) and homogenization temperatures (b) of pyrite-hosted fluid inclusions from the Yinjiagou deposit. Infrared light intensities (2, 4, 6, 8, 10 and 12) are controlled by the adjusting knob and approximately equal to the voltage values displayed by the LED indicator.

stage and Py-1 (Fig. 3), which demonstrates that, during phase separation, Fe and S preferentially entered into the hyper-saline liquid over the low density vapor.

5.2. Variation of He–Ar isotopes and sources of the ore-forming fluids

5.2.1. Variation of He–Ar isotopes

$^{40}Ar/^{36}Ar$ ratios of 465–1095 of the boiling fluids from Q–Mo (Py), QSP (Py) and Py-1 are slightly higher than those of 421–460 of the mixing fluid from Py-2. Both the nonlinearity of $^{40}Ar^*$ vs. $^{40}Ar/^{36}Ar$ (not shown) and the approximate linearity of $^{40}Ar/^{36}Ar$ and $^{3}He/^{36}Ar$ (Fig. 8b) generally exclude the effects of the *in situ* generation of ^{40}Ar due to the radioactive decay of K-bearing daughter minerals trapped in fluid inclusions of pyrite. However, considering that K-bearing daughter crystals are contained in some H type inclusions and that the initial ore-forming fluid might have a certain amount of K^+, the content of K is significant, and, thus, could produce considerable $^{40}Ar^*$, as reflected by the slight scatter of ^{40}Ar and $^{40}Ar^*$ on the

Table 2
Calibration results of typical fluid inclusions in pyrite from the Yinjiagou deposit.

Number	FI type (size)	Temperature (°C)	Infrared light intensity						Variation
			2	4	6	8	10	12	
1	L (80 μm)	T_{ice}	−4.2		−4.2	−4.3	−4.3	−4.5	−0.3
		T_{total}		291.6	291.6	291.8	291.6	291.5	0.3
2	L (60 μm)	T_{total}		304.5	304.4	304.2	303.5	303.2	1.3
3	L (40 μm)	T_{total}		305.5	305.7	305.4	305.2	305.0	0.5

L FI is liquid-rich biphase (LV) fluid inclusions. T_{ice} and T_{total} represent ice melting temperature and complete homogenization temperature, respectively. Infrared light intensities (2, 4, 6, 8, 10 and 12) are controlled by the adjusting knob and approximately equal to the voltage values displayed by the LED indicator.

Table 3
Noble gas compositions (E^{-9} cm³ STP g⁻¹) and isotopic ratios of fluid inclusions trapped in pyrite from the Yinjiagou deposit.

	No.	Stage	Weight (g)	^{4}He	^{40}Ar	^{40}Ar*	^{3}He/^{4}He (Ra)	Error	^{40}Ar/^{36}Ar	^{4}He/^{40}Ar*	F^{4}He	^{4}He$_{mantle}$ (wt.%)	T$_{total}$ (°C) (n)
HY1-7	1	Q–Mo (Py)	0.49	12.00	7.41	2.76	1.51	0.12	465.69	4.35	4367	17.8	397 ± 9 (26)
HY1-9	1	QSP (Py)	0.65	59.12	20.71	10.06	1.78	0.11	567.94	5.88	9388	21.8	375 ± 29 (34)
	2		0.65	10.94	2.26	1.37	1.39	0.12	745.37	7.97	20892	16.3	
	3		0.67	83.78	19.24	7.46	1.47	0.09	477.11	11.23	12030	17.3	
HY3-7	1	Py-1	0.73	5.33	4.32	3.17	5.26	0.35	1095.35	1.68	7825	65.3	ca. 380 ± 25[a]
	2		0.57	53.19	25.28	17.05	5.19	0.30	897.04	3.12	10929	64.4	
HY3-10	1	Py-2	0.66	23.31	12.58	4.04	0.80	0.06	430.18	5.77	4616	8.9	325 ± 28 (4)
	2		0.52	28.60	9.79	3.00	0.84	0.07	421.12	9.53	7124	9.4	
HY3-14	1	Py-2	0.73	12.20	16.77	5.68	2.40	0.17	441.84	2.15	1861	29.1	304 ± 20 (20)
	2		0.62	16.16	9.60	3.50	2.28	0.15	459.47	4.62	4479	27.6	

Numbers for the No. column represent multiple aliquots of the same sample. ^{40}Ar* is radiogenic ^{40}Ar given all of the Ar come from the fluid inclusions; ^{40}Ar* = ^{40}Ar–295.5 × ^{36}Ar. F^{4}He values reflect enrichment of ^{4}He in the fluid relative to air; F^{4}He = (^{4}He/^{36}Ar)$_{sample}$/(^{4}He/^{36}Ar)$_{air}$, where ^{4}He/^{36}Ar$_{air}$ = 0.1727 (Stuart et al., 1995). T$_{total}$ represents complete homogenization temperature. T$_{total}$ of fluid inclusions in Q–Mo (Q) and QSP (Q) are used to approximately represent T$_{total}$ of fluid inclusions in Q–Mo (Py) and QSP (Py).

[a] Uncertainty of homogenization temperatures of fluid inclusions in Py-1 is greatest owing to the infrared opacity under high temperatures.

mixing line (Figs. 8b and 9a). The radiogenic gas composition of the fluid endmembers can be reconstructed using mantle and crustal ^{3}He/^{4}He. Using a mantle endmember R/Ra = 8 (Fig. 9a), the undiluted mantle volatiles have ^{40}Ar*/^{4}He = 0.64 ± 0.16 (Fig. 9a). This is higher than the best estimated value of MORB mantle (0.49; Staudacher et al., 1989) and may reflect fractionation during phase separation or assimilation of crustal material prior to degassing, consistent with the higher ^{40}Ar*/^{3}He ratio of 86 ± 37 × 10³ compared with the mantle ^{40}Ar*/^{40}Ar ratio of 45 × 10³ (Moreira et al., 1998).

^{3}He/^{4}He ratios of the porphyry stage and the vein stage range from 1.39 to 1.78 Ra and from 0.80 to 5.26 Ra, respectively. Hearn et al. (1990) considered that extensive boiling could result in fractionation of ^{3}He into the vapor phase, with steam loss at the surface, whereas the boiling that affected our samples was most likely a small scale event with steam loss at depth. Simmons et al. (1987) suggested that preferential vapor-phase partitioning of ^{3}He could not account for the helium isotopic compositions at Pasto Bueno tungsten-base-metal-bearing deposit, Peru. In our study, the fluids of Q–Mo (Py) and QSP (Py) are both characteristic of boiling, whereas no notable differences are found between their ^{3}He/^{4}He ratios (Figs. 8a and 9), excluding the effect of fluid immiscibility. The remarkable difference of ^{3}He/^{4}He ratios between the porphyry and vein stages most likely represents two different fluid sources (Fig. 9; see below). Since all of the samples were collected at depth (100 to 250 m below the present surface), a contribution from cosmogenic ^{3}He can be ruled out. Furthermore, atmosphere-derived He is unlikely to affect He abundances and isotope compositions of crustal fluids, due to the insolubility of He in water and the low He concentration of the atmosphere (Ozima and Podosek, 2001). Therefore, the major sources of He in ore-forming fluids are the mantle and the crust. Crustal production of ^{3}He is dominated by the reaction ^{6}Li(n, α) → ^{3}H(β) → ^{3}He (Mamyrin and Tolstikhin, 1984). Because of the absence of any Li-rich phases in the study area, He production should have the same ^{3}He/^{4}He ratio as typical crust (<0.1 Ra). The ^{3}He/^{4}He ratios in Yinjiagou range from 0.80 to 5.26 Ra, considerably higher than that of He produced in the continental crust and provide clear evidence that both mantle-derived and crustal-derived (radiogenic) He is present in these ore-forming fluids. Additionally, the excellent correlation between ^{3}He/^{36}Ar and ^{40}Ar/^{36}Ar (Fig. 8b) also demonstrates that the ore-forming fluid can be considered as a combination of crustal and mantle components.

5.2.2. Sources of the ore-forming fluids

Crust and mantle contributions to ore-forming processes can often be traced using the fluid helium isotopic composition in the hydrothermal minerals, especially in pyrite. Many syngenetic and epigenetic metallic ore deposits have been reported as indicating the involvement of mantle-derived components based on helium

isotope studies (Simmons et al., 1987; Stuart et al., 1995; Hu et al., 1998; Mao et al., 2003; Burnard and Polya, 2004; Zhang L.C. et al., 2008). Given the simple, separate binary mixing in the porphyry and vein stages, the proportion of mantle ^{4}He is estimated from He$_{mantle}$ (%) = (R − Rc)/(Rm − Rc) × 100, where Rm, Rc and R represent the ^{3}He/^{4}He ratios of the fluids in the mantle, the crust and the samples, respectively. We use 8 Ra for Rm and a maximum 0.1 Ra for Rc omitting the impact of mantle and cosmogenic ^{3}He for Rc (Andrews, 1985); the actual Rc value is likely to be much lower than 0.1 Ra, based on the average crustal contents of Li (14 ppm), Th (8.2 ppm) and U (1.44 ppm) of the SMNCC (Zhang et al., 2001; Ballentine and Burnard, 2002). The mantle ^{4}He values of the porphyry stage range from 16 to 22%, while values of the vein stage range from 9 to 65% (Table 3). This mixture of mantle and crustal He should be related to the magmatic contribution. The participation of mantle fluids in the ore-forming fluids and the presence of a diluting fluid of crustal origin, have been previously proposed based on S, H and O isotopes (Chen and Fu, 1992; Wu, 2011). The values of δ^{34}S (−0.3‰–5.8‰) for fifty pyrite samples, δ^{18}O$_{H2O}$ (5.6‰–8.8‰) and δD$_{H2O}$ (−64‰ to −52‰) for quartz intergrown with pyrite all indicate a dominantly magmatic origin mixing with minor meteoric water. The involvement of mantle helium in this district was also reported from other deposits, resulting in the high ^{3}He/^{4}He ratios of 1.4–3.6 Ra from the Jinduicheng, Donggou, Shijiawan and Sandaozhuang deposits (Zhu et al., 2009) and the ^{3}He/^{4}He of 0.82 ± 0.41 Ra from gold deposits in adjacent Xiaoqinling district, SMNCC (Li et al., 2012).

Both the decreasing homogenization temperatures (Fig. 6) and the positive correlation of ^{3}He/^{36}Ar and ^{40}Ar/^{36}Ar (Fig. 8b) of various veins reflect an increasing dilution of a magmatic fluid by low temperature meteoric water in the hydrothermal system. The magmatic fluid ^{3}He/^{4}He and ^{40}Ar/^{36}Ar are below typical mantle values. For helium isotopes this represents a mixture of radiogenic and mantle derived He. The mantle He has likely exsolved from mantle derived calc-alkaline magmas. The intercept of a best-fit line in Fig. 8b identifies a ^{40}Ar/^{36}Ar of 390 for the crustal fluid component, which is higher than atmospheric Ar, representing a meteoric fluid component within a small volume of crustal radiogenic ^{40}Ar. Fig. 9 defines two different trends and radiogenic isotopic ratios of the endmembers. One is for the porphyry stage with relatively constant ^{3}He/^{4}He ratios, of magmatic origin with initial R/Ra of ca. 1.8 and mantle ^{4}He of 22%. The Yinjiagou K-feldspar granite porphyry has low ^{87}Sr/^{86}Sr ratios (0.7074–0.7082; Chen and Fu, 1992; Li et al., 2013), characteristic of I-type granites, which are largely produced by partial melting of the lower crust. The initial fluid of the porphyry stage should emanate from the cooling intrusions (K-feldspar granite porphyry) at depth. The relatively constant R/Ra from the porphyry stage could represent the isotopic characteristics of deep magma (perhaps K-spar granite porphyry). Another trend for the later vein stage indicates a mixing relationship. The highest ^{3}He/^{4}He (5.26 Ra) of fluid inclusions in Py-1 is close to

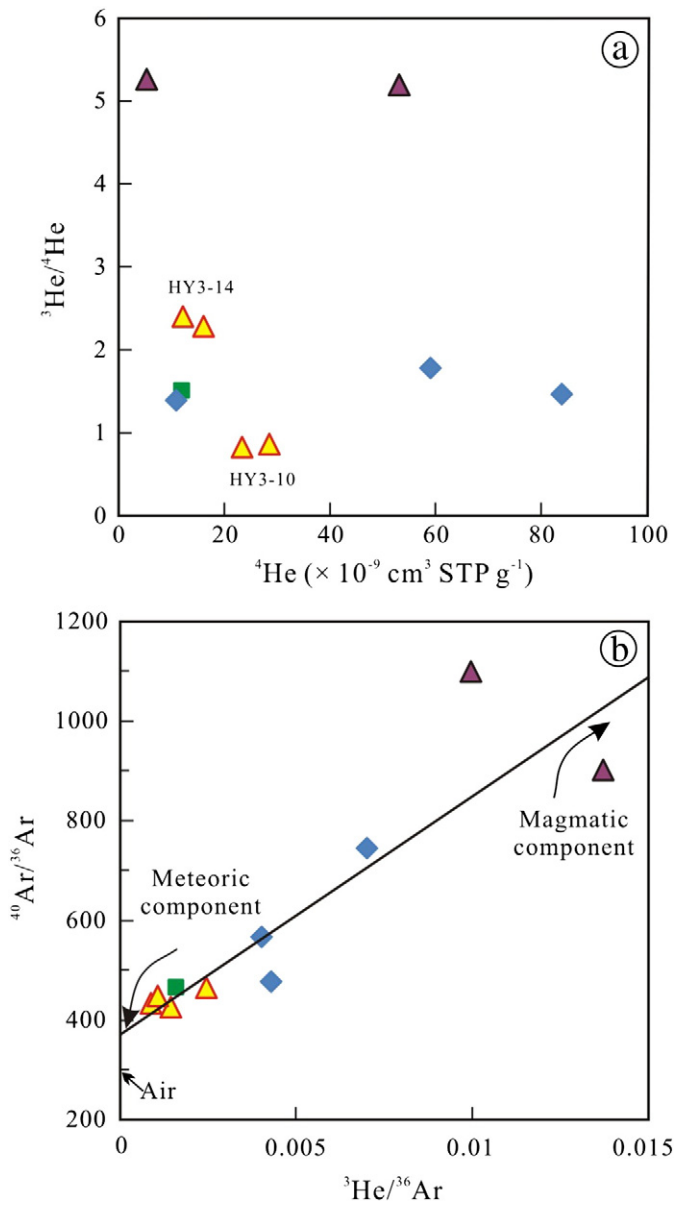**Fig. 8.** Graphs of ^{4}He vs. ^{3}He/^{4}He (a) and ^{3}He/^{36}Ar vs. ^{40}Ar/^{36}Ar (b) of pyrite-hosted fluid inclusions from Yinjiagou deposit. Square filled with green and diamonds filled with blue represent Q–Mo (Py) and QSP (Py) of porphyry stage, respectively. Black triangles filled with purple and red triangles filled with yellow represent Py-1 and Py-2 of vein stage, respectively. The magmatic component is characterized by the presence of both ^{40}Ar and ^{3}He. The low ^{40}Ar/^{36}Ar–^{3}He/^{36}Ar component represents a meteoric fluid component (^{40}Ar/^{36}Ar = 390) and variable amounts of atmospheric noble gases (^{40}Ar/^{36}Ar = 298, ^{3}He/^{36}Ar = 2 × 10^{-7}).

Fig. 9. ^{40}Ar*/^{4}He vs. ^{3}He/^{4}He (a) and ^{40}Ar/^{36}Ar vs. ^{3}He/^{4}He (b) of various veins. Symbols as in Fig. 8. Two different trends with endmembers with different isotopic compositions are defined. One is for the porphyry stage with relatively constant ^{3}He/^{4}He ratios, of magmatic origin with initial R/Ra = 1.8, representing the isotopic characteristics of deep magma (perhaps K-spar granite porphyry). Another is for the vein stage, indicating a mixing relationship and representing a different magmatic sourced hydrothermal system mixed with a low ^{3}He/^{4}He surface-derived fluid.

5.3. Possible mineralization model

The combination of the ^{3}He/^{4}He and temperature results allows us to further trace the fluid evolution. The temperatures are presented as the averages of fluid inclusions in each sample with a 1 sigma standard deviation. Because we could not directly obtain temperatures for the fluid inclusions in Q–Mo (Py) and QSP (Py), because of the intergrowth relationship between quartz and pyrite (Fig. 2a and b), the homogenization temperatures of fluid inclusions in the Q–Mo (Q) and QSP (Q) are used to approximately represent the temperatures of fluid inclusions in the Q–Mo (Py) and QSP (Py). An interesting relationship is observed between ^{3}He/^{4}He and homogenization temperature (Fig. 10). The ratios of ^{3}He/^{4}He from the porphyry stage are relatively uniform and low, with relatively high homogenization temperatures, whereas the ^{3}He/^{4}He ratios from the vein stage form an approximately linear relationship with the homogenization temperatures. Although the cause of the difference

the ratio of subcontinental mantle (6 Ra; Gautheron and Moreira, 2002). The fluid from Py-1 with mantle ^{4}He of 65% must represent another individual magmatic sourced hydrothermal system (as opposed to the porphyry ore-forming system), which might be attributed to a later, more mafic magmatic event. This conjecture has been confirmed by the latest geochronology study (see below). The notable variation in R/Ra from Py-1 to Py-2 similar to the helium isotopic variation in most sulfides from hydrothermal deposits analyzed to date (e.g., Stuart et al., 1995; Hu et al., 1998; Kendrick et al., 2001; Mao et al., 2003), reflects the mixing (Figs. 6 and 9) of the mantle-derived fluid with a low ^{3}He/^{4}He diluted fluid undoubtedly containing a surface-derived radiogenic crustal helium.

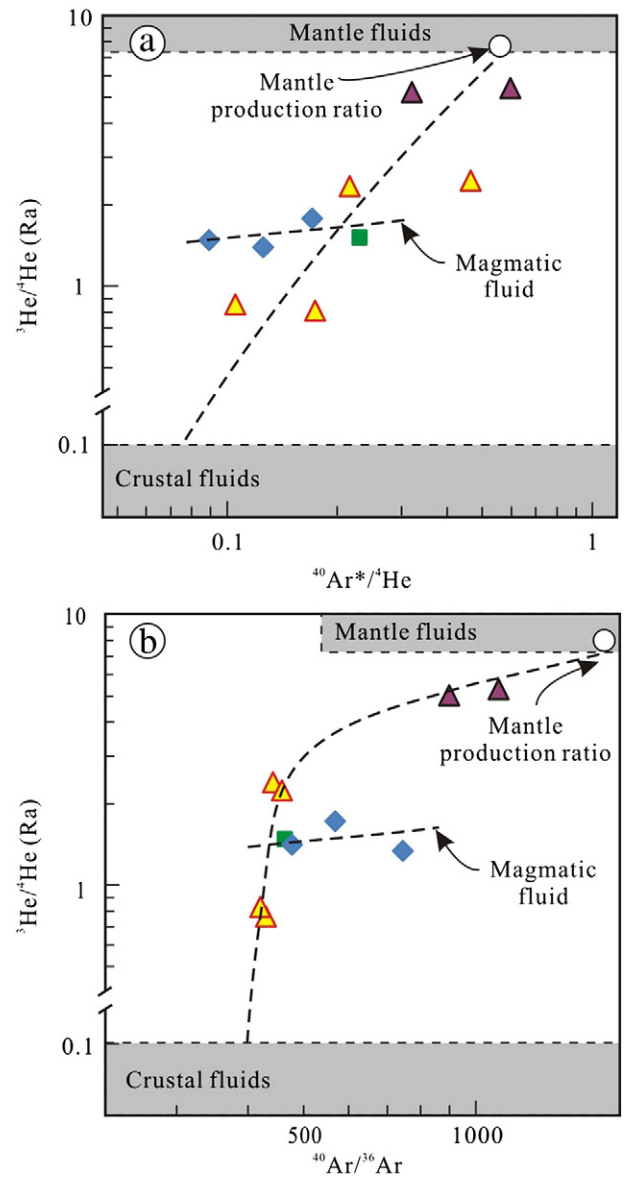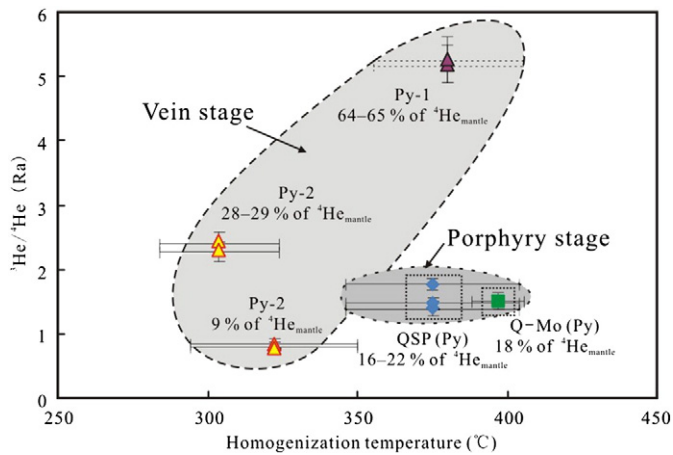**Fig. 10.** Homogenization temperature and $^3He/^4He$ graph of various mineralized veins from the Yinjiagou deposit. Symbols as Fig. 8. The homogenization temperatures of fluid inclusions in the Q–Mo (Q) and QSP (Q) are used to approximately represent the temperatures of fluid inclusions in these pyrites. R/Ra from porphyry stage are relatively uniform and low, with relatively high homogenization temperatures, whereas R/Ra from vein stage form an approximately linear relationship with the homogenization temperatures, reflecting their different fluid sources and evolutionary paths.

is uncertain, we speculate that it might also reflect two different fluid sources and evolutionary paths. This speculation is consistent with the field observation that the veinlet molybdenite of the porphyry stage was formed before the veined pyrite–chalcopyrite; the former occurs in the K-feldspar granite porphyry, whereas the latter occurs in the K-feldspar granite porphyry and quartz diorite porphyry, locally cutting the molybdenite ore bodies. This result is also consistent with a Re–Os age of 146 ± 1.1 Ma for the molybdenite mineralization (Wu, 2011) and a slightly younger age of 141 ± 1.1 Ma for the pyrite mineralization based on both zircon U–Pb and pyrite Re–Os ages of the quartz–pyrite veins (Zhu et al., 2013).

Our microthermometric and He–Ar isotopic results favor a multi-stage model for the Yinjiagou poly-metallic deposit. The initial medium density and salinity fluid of the porphyry stage, with temperature more than 420 °C, which emanates from K-feldspar granite porphyry at depth, contains ca. 20% mantle helium. As this fluid migrated upwards, boiling occurred due to the decompression and associated cooling and resulted in molybdenite precipitation. The QSP veins are widely distributed along the roof and floor of the ore bodies, most likely representing pressure release zones and late fluid flow channels, similar to the Big Gossan Cu–Au skarn deposit in Irian Jaya (Meinert et al., 1997) and the Far Southeast-Lepanto porphyry and epithermal Cu–Au deposits in the Philippines (Hedenquist et al., 1998). After the development of the K-feldspar granite and/or quartz diorite porphyries, another magmatic event occurred, which produced new hydrothermal fluid (s) involving approximately 65% mantle helium with temperature more than 350 °C. During the upward migration of this fluid along the fractured weak zones (perhaps the QSP veins), boiling occurred. The fluid then mixed with a low $^3He/$ ^4He surface-derived fluid. Continued addition of a crustal component during deposition further lowered the temperature below 350 °C and diluted the $^3He/^4He$ to 2.4 Ra and 0.8 Ra for the main pyrite deposit, reflecting the increasing importance of the meteoric component as mineralization proceeded. Mixing and diluting could account for the significant variation in the R/Ra of the vein stage and resulted in a large amount of pyrite precipitating, forming the most economically important pyrite in Yinjiagou.

5.4. Implications for the regional tectonic setting

The large scale metallogenesis in the SMNCC is related to a series of Mesozoic granitoid plutons that were triggered by the transformation

of the tectonic regime during the Late Jurassic to Early Cretaceous periods. The initial $^{87}Sr/^{88}Sr$ ratios (0.7061–0.7100) of these intrusions suggest either mixed mantle and crustal sources or derivation from partial melting of the lower crust (Chen et al., 2000; Zhang et al., 2009; Mao et al., 2011; and references therein) in an extensional setting (e.g., Ratschbacher et al., 2003; Mao et al., 2008; Ling et al., 2009; Li et al., 2012). The extensional setting related to the lithospheric modification and thinning in the western (Xiaoqinling) and eastern parts of the NCC has been described based on the geochemistry of numerous metamorphic core complexes, intra-continental rift-basins and felsic and mafic intrusions (Wu et al., 2008; Li et al., 2012; and references therein) and on the geophysics (Chen et al., 2008; Xu et al., 2011; Zhu et al., 2011). Lithospheric extension and asthenospheric upwelling caused extensive mantle-derived magmatism and could have provided sufficient fluids, sulfur and other components to form the poly-metallic province in the SMNCC (Fig. 1a). The transport of mantle volatiles through the crust is closely linked to the tectonic setting; mantle ^3He in groundwater is typically found in regions of crustal extension, and is thought to be released during the intrusion of subsurface melts that are associated with the extension (Oxburgh et al., 1986). Hence, the high $^3He/^4He$ ratios of the Yinjiagou deposit indicate an intense extensional setting, which may be attributed to Late Jurassic to Early Cretaceous lithospheric modification and thinning of the SMNCC. This setting would explain the emplacement of the large-scale pyrite mineralization in the East Qinling metallogenic belt.

6. Conclusions

Geologic, petrographic, fluid inclusion and He–Ar isotopic evidence indicate different fluid sources and evolutionary processes between porphyry molybdenite mineralization and vein pyrite–chalcopyrite deposition in the Yinjiagou ore district. The hydrothermal evolution was controlled by the Yanshanian complex intrusions and involved fluids of mixed crust–mantle origin. Hydrothermal processes occurred during boiling, progressive cooling and mixing as recorded by the fluid inclusions. Fluid immiscibility is not only an important factor for the precipitation of molybdenite but also concentrates the content of Fe and S. For the vein stage, both fluid features and He–Ar isotopic compositions indicate that an individual hydrothermal fluid dominated by a mantle component, much larger than the mantle component in the porphyry ore-forming system, mixed to various extents with crustally derived fluids. This mixing process was the main factor leading to the precipitation of the most economically important pyrite. The high $^3He/^4He$ ratios imply a strongly extensional setting.

References

Andrews, J.N., 1985. The isotopic composition of radiogenic helium and its use to study groundwater movement in confined aquifers. Chemical Geology 49, 339–351.
Audétat, A., Pettke, T., 2003. The magmatic-hydrothermal evolution of two barren granites: a melt and fluid inclusion study of the Rito del Medio and Cañada Pinabete plutons in northern New Mexico (USA). Geochimica et Cosmochimica Acta 67, 97–121.
Ballentine, C.J., Burnard, P.G., 2002. Production, release and transport of noble gases in the continental crust. Reviews in Mineralogy and Geochemistry 47, 481–538.

Ballentine, C.J., Burgess, R., Marty, B., 2002. Tracing fluid origin, transport and interaction in the crust. Reviews in Mineralogy and Geochemistry 47, 539–614.

Bodnar, R.J., 1985. Fluid inclusion systematics in epithermal systems. Reviews in Economic Geology 2, 73–97.

Bodnar, R., 1993. Revised equation and table for determining the freezing point depression of H_2O – Nacl solutions. Geochimica et Cosmochimica Acta 57, 683–684.

Boyle, A.P., Prior, D.J., Banham, M.H., Timms, N.E., 1998. Plastic deformation of metamorphic pyrite: new evidence from electron-backscatter diffraction and forescatter orientation-contrast imaging. Mineralium Deposita 34, 71–81.

Burnard, P.G., Polya, D.A., 2004. Importance of mantle derived fluids during granite associated hydrothermal circulation: He and Ar isotopes of ore minerals from Panasqueira. Geochimica et Cosmochimica Acta 68, 1607–1615.

Burnard, P.G., Graham, D., Turner, G., 1997. Vesicle-specific noble gas analyses of "popping rock": implications for primordial noble gases in earth. Science 276, 568–571.

Burnard, P.G., Hu, R., Turner, G., Bi, X.W., 1999. Mantle, crustal and atmospheric noble gases in ailaoshan gold deposits, Yunnan Province, China. Geochimica et Cosmochimica Acta 63, 1595–1604.

Campbell, A.R., Robinson-Cook, S., 1987. Infrared fluid inclusion microthermometry on coexisting wolframite and quartz. Economic Geology 82, 1640–1645.

Campbell, A.R., Hackbarth, C.J., Plumlee, G.S., Petersen, U., 1984. Internal features of ore minerals seen with the infrared microscope. Economic Geology 79, 1387–1392.

Chen, Y.J., Fu, S.G., 1992. Mineralization of Gold Deposits in West Henan, China. China Seismological Press, Beijing (234 pp. (in Chinese)).

Chen, Y.J., Wang, Y., 2010. Fluid inclusion study of the Tangjiaping Mo deposit, Dabie Shan, Henan Province: implications for the nature of the porphyry systems of post-collisional tectonic settings. International Geology Review 53, 635–655.

Chen, Y.J., Li, C., Zhang, J., Li, Z., Wang, H.H., 2000. Sr and O isotopic characteristics of porphyries in the Qinling molybdenum deposit belt and their implication to genetic mechanism and type. Science in China (Series D: Earth Sciences) 30, 82–94 (in Chinese).

Chen, Y.J., Chen, H.Y., Zaw, K., Pirajno, F., Zhang, Z.J., 2007. Geodynamic settings and tectonic model of skarn gold deposits in China: an overview. Ore Geology Reviews 31, 139–169.

Chen, L., Tao, W., Zhao, L., Zheng, T., 2008. Distinct lateral variation of lithospheric thickness in the Northeastern North China Craton. Earth and Planetary Science Letters 267, 56–68.

Chen, Y.J., Pirajno, F., Li, N., Guo, D.S., Lai, Y., 2009. Isotope systematics and fluid inclusion studies of the Qiyugou breccia pipe-hosted gold deposit, Qinling Orogen, Henan province, China: implications for ore genesis. Ore Geology Reviews 35, 245–261.

Ding, L.-X., Ma, C.-Q., Li, J.-W., Robinson, P.T., Deng, X.-D., Zhang, C., Xu, W.-C., 2011. Timing and genesis of the adakitic and shoshonitic intrusions in the Laoniushan complex, southern margin of the North China Craton: implications for post-collisional magmatism associated with the Qinling Orogen. Lithos 126, 212–232.

Dong, Y., Zhang, G., Neubauer, F., Liu, X., Genser, J., Hauzenberger, C., 2011. Tectonic evolution of the Qinling orogen, China: review and synthesis. Journal of Asian Earth Sciences 41, 213–237.

Driesner, T., Heinrich, C., 2007. The system H_2O – NaCl. Part I: Correlation formulae for phase relations in temperature–pressure–composition space from 0 to 1000 °C, 0 to 5000 bar, and 0 to 1 XNaCl. Geochimica et Cosmochimica Acta 71, 4880–4901.

Gautheron, C., Moreira, M., 2002. Helium signature of the subcontinental lithospheric mantle. Earth and Planetary Science Letters 199, 39–47.

Ge, X., Su, W.C., Zhu, L.Y., Wu, L.Y., 2011. A study on the influence of infrared light source intensity on salinity of fluid inclusion in opaque mineral by using infrared microthermometry: in the case of stibnite. Acta Mineralogica Sinica 31, 366–371 (in Chinese with English abstract).

Giggenbach, W.F., Stewart, M.K., 1982. Processes controlling the isotopic composition of steam and water discharges from steam vents and steam-heated pools in geothermal areas. Geothermics 11, 71–80.

Goldstein, R.H., Reynolds, T.J., 1994. Systematics of fluid inclusions in diagenetic minerals. Society for sedimentary geology. SEPM Short Course, 31 183.

Hagemann, S., Lüders, V., 2003. P–T–X conditions of hydrothermal fluids and precipitation mechanism of stibnite-gold mineralization at the Wiluna lode-gold deposits, Western Australia: conventional and infrared microthermometric constraints. Mineralium Deposita 38, 936–952.

Hall, D.L., Sterner, S.M., Bodnar, R.J., 1988. Freezing point depression of NaCl – KCl – H_2O solutions. Economic Geology 83, 197–202.

He, Y.H., Zhao, G.C., Sun, M., Wilde, S.A., 2008. Geochemistry, isotope systematics and petrogenesis of the volcanic rocks in the Zhongtiao Mountain: an alternative interpretation for the evolution of the southern margin of the North China Craton. Lithos 102, 158–178.

He, H.Y., Zhu, R.X., Saxton, J., 2011. Noble gas isotopes in corundum and peridotite xenoliths from the eastern North China Craton: implication for comprehensive refertilization of lithospheric mantle. Physics of the Earth and Planetary Interiors 189, 185–191.

Hearn, E.H., Kennedy, B.M., Truesdell, A.H., 1990. Coupled variations in helium isotopes and fluid chemistry: Shoshone Geyser Basin, Yellowstone National Park. Geochimica et Cosmochimica Acta 54, 3103–3113.

Hedenquist, J.W., Henley, R.W., 1985. The importance of CO_2 on freezing point measurements of fluid inclusions; evidence from active geothermal systems and implications for epithermal ore deposition. Economic Geology 80, 1379–1406.

Hedenquist, J.W., Arribas, A., Reynolds, T.J., 1998. Evolution of an intrusion-centered hydrothermal system; Far Southeast-Lepanto porphyry and epithermal Cu – Au deposits, Philippines. Economic Geology 93, 373–404.

Heinrich, C.A., Gunther, D., Audetat, A., Ulrich, T., Frischknecht, R., 1999. Metal fractionation between magmatic brine and vapor, determined by microanalysis of fluid inclusions. Geology 27, 755–758.

Hu, R.Z., Burnard, P.G., Turner, G., Bi, X., 1998. Helium and Argon isotope systematics in fluid inclusions of Machangqing copper deposit in west Yunnan province, China. Chemical Geology 146, 55–63.

Hu, R.Z., Bi, X.W., Turner, G., Burnard, P., 1999. He – Ar isopotic geochemistry of the ore-forming fluid from the Ailaoshan gold ore belt. Science in China, Series D 29, 321–330 (in Chinese).

Jean-Baptiste, P.H., Fouquet, Y., 1996. Abundance and isotopic composition of helium in hydrothermal sulfides from the East Pacific Rise at 13 °N. Geochimica et Cosmochimica Acta 60, 87–93.

Kendrick, M.A., Burnard, P., 2013. Noble gases and halogens in fluid inclusions: a journey through the earth's crust. In: Burnard, P. (Ed.), The Noble Gases as Geochemical Tracers. Springer, Heidelberg, pp. 319–370.

Kendrick, M.A., Burgess, R., Pattrick, R.A.D., Turner, G., 2001. Fluid inclusion noble gas and halogen evidence on the origin of Cu-Porphyry mineralising fluids. Geochimica et Cosmochimica Acta 65, 2651–2668.

Kouzmanov, K., Bailly, L., Ramboz, C., Rouer, O., Bény, J.-M., 2002. Morphology, origin and infrared microthermometry of fluid inclusions in pyrite from the Radka epithermal copper deposit, Srednogorie zone, Bulgaria. Mineralium Deposita 37, 599–613.

Kouzmanov, K., Pettke, T., Heinrich, C.A., 2010. Direct analysis of ore-precipitating fluids: combined IR Microscopy and LA-ICP-MS study of fluid inclusions in opaque ore minerals. Economic Geology 105, 351–373.

Li, S.G., Hart, S.R., Zheng, S.G., Guo, A.L., Liu, D.L., Zhang, G.W., 1989. The collision time of North China plate and South China plate: evidence from Sm – Nd ages. Science in China, Series D 19, 312–319 (in Chinese).

Li, N., Chen, Y.J., Zhang, H., Zhao, T.P., Deng, X.H., Wang, Y., Ni, Z.Y., 2007. Molybdenum deposits in East Qinling. Earth Science Frontiers 14, 186–198 (in Chinese with English abstract).

Li, J.-W., Bi, S.-J., Selby, D., Chen, L., Vasconcelos, P., Thiede, D., Zhou, M.-F., Zhao, X.-F., Li, Z.-K., Qiu, H.-N., 2012. Giant Mesozoic gold provinces related to the destruction of the North China craton. Earth and Planetary Science Letters 349–350, 26–37.

Li, T.G., Wu, G., Chen, Y.C., Li, Z.Y., Yang, X.S., Qiao, C.J., 2013. Geochronology, geochemistry and petrogenesis of the Yinjiagou complex in western Henan Province, China. Acta Petrologica Sinica 29, 46–66 (in Chinese with English abstract).

Lindaas, S.E., Kulis, J., Campbell, A.R., 2002. Near-infrared observation and microthermometry of pyrite-hosted fluid inclusions. Economic Geology 97, 603–618.

Ling, M.-X., Wang, F.-Y., Ding, X., Hu, Y.-H., Zhou, J.-B., Zartman, R.E., Yang, X.-Y., Sun, W., 2009. Cretaceous ridge subduction along the lower Yangtze River belt, eastern china. Economic Geology 104, 303–321.

Lüders, V., Ziemann, M., 1999. Possibilities and limits of infrared light microthermometry applied to studies of pyrite-hosted fluid inclusions. Chemical Geology 154, 169–178.

Luo, M.J., Zhang, F.M., Dong, Q.Y., Xu, Y.R., Li, S.M., Li, K.H., 1991. Molybdenum Deposits in China. Henan Press of Science and Technology, Zhengzhou (452 pp. (in Chinese)).

Mamyrin, B.A., Tolstikhin, I.N., 1984. Helium isotopes in nature. Elsevier, Amsterdam (273 pp.).

Mao, J.W., Li, Y.Q., Goldfarb, R., He, Y., Zaw, K., 2003. Fluid inclusion and noble gas studies of the Dongping Gold Deposit, Hebei Province, China: a mantle connection for mineralization? Economic Geology 98, 517–534.

Mao, J.W., Xie, G.Q., Bierlein, F., Qü, W.J., Du, A.D., Ye, H.S., Pirajno, F., Li, H.M., Guo, B.J., Li, Y.F., Yang, Z.Q., 2008. Tectonic implications from Re – Os dating of Mesozoic molybdenum deposits in the East Qinling–Dabie orogenic belt. Geochimica et Cosmochimica Acta 72, 4607–4626.

Mao, J.W., Ye, H.S., Wang, R.T., Dai, J.Z., Jian, W., Xiang, J.F., Zhou, K., Meng, F., 2009. Mineral deposit model of Mesozoic porphyry Mo and vein type Pb – Zn – Ag ore deposits in the East Qinling, Central China and its implication for prospecting. Geological Bulletin of China 29, 72–79 (in Chinese with English abstract).

Mao, J.W., Pirajno, F., Xiang, J.F., Gao, J.J., Ye, H.S., Li, Y.F., Guo, B.J., 2011. Mesozoic molybdenum deposits in the east Qinling–Dabie orogenic belt: characteristics and tectonic settings. Ore Geology Reviews 43, 264–293.

Meinert, L.D., Hefton, K.K., Mayes, D., Tasiran, I., 1997. Geology, zonation, and fluid evolution of the Big Gossan Cu – Au skarn deposit, Ertsberg District, Irian Jaya. Economic Geology 92, 509–534.

Meng, Q.R., Zhang, G.W., 1999. Timing of collision of the North and South China blocks: controversy and reconciliation. Geology 27, 123–126.

Moreira, M., Kunz, J., Allègre, C., 1998. Rare gas systematics in popping rock: isotopic and elemental compositions in the upper mantle. Science 279, 1178–1181.

Moritz, R., 2006. Fluid salinities obtained by infrared microthermometry of opaque minerals: Implications for ore deposit modeling—a note of caution. Journal of Geochemical Exploration 89, 284–287.

Oxburgh, E.R., O'Nions, R.K., Hill, R.I., 1986. Helium isotopes in sedimentary basins. Nature 324, 632–635.

Ozima, M., Podosek, F.A., 2001. Noble gas geochemistry. Cambridge University Press (367 pp.).

Peng, P., Zhai, M., Ernst, R.E., Guo, J., Liu, F., Hu, B., 2008. A 1.78 Ga large igneous province in the North China craton: the Xiong'er Volcanic Province and the North China dyke swarm. Lithos 101, 260–280.

Philippot, P., Ménez, B., Simionovici, A., Chabiron, A., Cuney, M., Snigirev, A., Snigireva, I., 2000. X-ray imaging of uranium in individual fluid inclusions. Terra Nova 12, 84–89.

Pirajno, F., Ernst, R.E., Borisenko, A.S., Fedoseev, G., Naumov, E.A., 2009. Intraplate magmatism in Central Asia and China and associated metallogeny. Ore Geology Reviews 35, 114–136.

Pokrovski, G.S., Roux, J., Harrichoury, J.C., 2005. Fluid density control on vapor–liquid partitioning of metals in hydrothermal systems. Geology 33, 657–660.

Ratschbacher, L., Hacker, B.R., Calvert, A., Webb, L.E., Grimmer, J.C., McWilliams, M.O., Ireland, T., Dong, S., Hu, J., 2003. Tectonics of the Qinling (Central China): tectonostratigraphy, geochronology, and deformation history. Tectonophysics 366, 1–53.

Redmond, P.B., Einaudi, M.T., Inan, E.E., Landtwing, M.R., Heinrich, C.a, 2004. Copper deposition by fluid cooling in intrusion-centered systems: new insights from the Bingham porphyry ore deposit, Utah. Geology 32, 217–220.

Ren, J.S., Chen, T.Y., Niu, B.G., 1992. Tectonic Evolution of the Continental Lithosphere of the East China and Adjacent Area and Relevant Mineralization. Science Press, Beijing (230 pp. (in Chinese)).

Richards, J.P., Kerrich, R., 1993. Observations of zoning and fluid inclusions in pyrite using a transmitted infrared light microscope (Lambda < or = 1.9 mu m). Economic Geology 88, 716–723.

Richards, J.P., Kerrich, R., 1993. The Porgera gold mine, Papua New Guinea; magmatic hydrothermal to epithermal evolution of an alkalic-type precious metal deposit. Economic Geology 88, 1017–1052.

Sano, Y., Marty, B., Burnard, P., 2013. Noble gases in the atmosphere. In: Burnard, P. (Ed.), The Noble Gases as Geochemical Tracers. Springer, Heidelberg, pp. 17–32.

Seo, J.H., Guillong, M., Heinrich, C.A., 2009. The role of sulfur in the formation of magmatic-hydrothermal copper–gold deposits. Earth and Planetary Science Letters 282, 323–328.

Shepherd, T.J., Rankin, A.H., Alderton, D.H.M., 1985. A Practical Guide to Fluid Inclusion Studies. Blackie, London 239 pp.

Simmons, S.F., Sawkins, F.J., Schlutter, D.J., 1987. Mantle-derived helium in two Peruvian hydrothermal ore deposits. Nature 329, 429–432.

Simon, A.C., Pettke, T., Candela, P.A., Piccoli, P.M., Heinrich, C.A., 2004. Magnetite solubility and iron transport in magmatic–hydrothermal environments. Geochimica et Cosmochimica Acta 68, 4905–4914.

Simon, A.C., Frank, M.R., Pettke, T., Candela, P.A., Piccoli, P.M., Heinrich, C.A., 2005. Gold partitioning in melt–vapor–brine systems. Geochimica et Cosmochimica Acta 69, 3321–3335.

Staudacher, T., Sarda, P., Richardson, S., Allegre, C.J., Sagna, I., Dimitriev, L.V., 1989. Noble gases in basalts from a mid-Atlantic ridge topographic high at 14°N: geodynamic consequences. Earth and Planetary Science Letters 96, 119–133.

Stuart, F.M., Turner, G., Duckworth, R.C., Fallick, A.E., 1994. Helium isotopes as tracers of trapped hydrothermal fluids in ocean-floor sulfides. Geology 22, 823–826.

Stuart, F.M., Burnard, P.G., Taylor, R.P., Turner, G., 1995. Resolving mantle and crustal contributions to ancient hydrothermal fluids: He–Ar isotopes in fluid inclusions from Dae Hwa W–Mo mineralisation, South Korea. Geochimica et Cosmochimica Acta 59, 4663–4673.

Williams-Jones, A.E., Heinrich, C.A., 2005. 100th Anniversary Special Paper: vapor transport of metals and the formation of magmatic–hydrothermal ore deposits. Economic Geology 100, 1287–1312.

Wu, G., 2011. Polymetallic metallogenic regularity and prognosis studies of the Yinjiagou area, Henan provience. (Post Doctorate Outbound Report Thesis) Institute of Mineral Resources, Chinese Academy of Geological Sciences.

Wu, F.Y., Xu, Y.G., Gao, S., Zheng, J.P., 2008. Lithospheric thinning and destruction of the North China Craton. Acta Petrologica Sinica 24, 1145–1174 (in Chinese with English abstract).

Xu, W.W., Zheng, T.Y., Zhao, L., 2011. Mantle dynamics of the reactivating North China Craton: constraints from the topographies of the 410-km and 660-km discontinuities. Science China: Earth Sciences 54, 881–887.

York, D., Masliwec, A., Kuybida, P., Hanes, J.A., Hall, C.M., Kenyon, W.J., Spooner, E.T.C., Scott, S.D., 1982. $^{40}Ar/^{39}Ar$ dating of pyrite. Nature 300, 52–53.

Zhang, G.W., Meng, Q.R., Yu, Z.P., Sun, Y., Zhou, D.W., Guo, A.L., 1996. Orogenesis and dynamics of the Qinling Orogen. Science in China, Series D 39, 225–234.

Zhang, G.W., Zhang, B.R., Yuan, X.C., Chen, J.Y., 2001. Qinling Orogenic Belt and Continental Dynamics. Science Press, Beijing (855 pp. (in Chinese with English abstract)).

Zhang, L.C., Zhou, X.H., Ding, S.J., 2008. Mantle-derived fluids involved in large-scale gold mineralization, Jiaodong District, China: constraints provided by the He–Ar and H–O isotopic systems. International Geology Review 50, 472–482.

Zhang, X.M., Qiao, C.J., Cai, X.D., Zhang, X.W., Wang, W.L., Zhang, C.H., Zhang, Y.H., 2008. Characteristics of Yinjiagou polymetal-pyrite deposit related to pulse magmatic intrusions in Henan, China. Global Geology 27, 137–145 (in Chinese with English abstract).

Zhang, Z., Yang, X., Dong, Y., Zhu, B., Chen, D., 2009. Molybdenum deposits in the eastern Qinling, central China: constraints on the geodynamics. International Geology Review 53, 261–290.

Zhu, B.Q., 1998. Study on chemical heterogeneities of mantle–crustal systems and geochemical boundaries of blocks. Earth Science Frontiers 5, 72–82 (in Chinese with English abstract).

Zhu, L.M., Zhang, G.W., Guo, B., Li, B., 2009. He–Ar isotopic system of fluid inclusions in pryite from the molybdenum deposits in south margin of North China Block and its trace to metallogenecit and geodynamic background. Chinese Science Bulletin 54, 1725–1735.

Zhu, R.X., Chen, L., Wu, F.Y., Liu, J.L., 2011. Timing, scale and mechanism of the destruction of the North China Craton. Science China: Earth Sciences 54, 789–797.

Zhu, M.T., Zhang, L.C., Wu, G., Jin, X.D., Xiang, P., Li, W.J., 2013. Zircon U–Pb and pyrite Re–Os age constraints on pyrite mineralization in the Yinjiagou deposit, China. International Geology Review. http://dx.doi.org/10.1080/00206814.2013.786313.